Chapter 8 :

Étude de la région riche en trous dans les composés de la famille $Bi_{1-x}Ca_xMnO_3$

8 Étude de la région riche en trous dans les composés de la famille $Bi_{1-x}Ca_xMnO_3$

Dans ce chapitre, nous présentons une étude systématique sur des composés fortement dopés en trous de la famille $Bi_{1-x}Ca_xMnO_3$ (x [1/2-0.875]. Leurs diagrammes de phase ont été étudiés en utilisant des techniques de diffraction à haute résolution, de transport électrique et des mesures magnétiques d'aimantation. L'effet du Bi^{+3} a été étudié grâce à l'étude comparative avec des composées à base de La^{+3}. La coexistence de différentes phases avec de l'ordre orbital dans le composé x=2/3 et la coexistence de phases dans x=0.85 et x=0.875 sont décrites. Des résultats nouveaux, basés sur l'analyse combinée de mesures de diffraction de neutrons (NPD) et de rayons X au synchrotron (SXRPD), ont été trouvés concernant la quasi-dégénération de l'ordre orbital et la ségrégation des phases dans les composés fortement dopés qui présentent de la MR.

8 Hole rich region of $Bi_{1-x}Ca_xMnO_3$ oxides

In this chapter, we present a systematic study on the highly hole doped region (x [1/2-0.875]) of the family $Bi_{1-x}Ca_xMnO_3$. The phase diagram has been investigated using high-resolution powder diffraction techniques, electrical transport, and magnetic measurements.

The effect of Bi^{+3} has been studied on the light of the reported studies based on La^{+3} substituted manganites. The coexistence of different orbital ordering phases in x=2/3 compound and the phase coexistence in x=0.85 and x=0.875 has been fully described in bismuth based compounds. Unprecedented results based on joint NPD and SXRPD concerning the quasi-degenerate orbital ordering and the phase segregation in highly doped compounds exhibiting MR are also described in detail.

8.1 Introduction

Most of the experimental work on CMR materials has been performed on electron rich manganites which constitutes the doping range where the maximum CMR was observed. Nevertheless, it has recently appeared an increasing interest on the hole rich region.

The conventional double-exchange model [13] for Mn oxides predicts FM phases around the x=0.5 doping, but that is inconsistent with the AFM phases for x>0.5 observed experimentally [190]. Additional terms are needed to extend the DE theory as for example: the Jahn Teller effect [38, 191], the order-disorder effect [192], orbital degrees of freedom [158, 193, 194] and Coulomb interaction [195]. In addition, the behaviour of doped manganites with x<1/2 and x>1/2 is dramatically different. In particular, for x>1/2, stable phases have been observed with long structural periods determined by the doping (κ=(0,1-x,0) [235]). While no long period structures have been observed for x<1/2 except in the case of phase segregated phenomena reported for x<1/2.

From the electronic point of view, some authors [190] have considered the problem of Double Exchange via degenerate orbitals in highly hole doped compounds. They argued that in order to understand the highly hole doped region it is necessary to take into account that, when doping the end member compound $CaMnO_3$, the carriers are introduced into degenerate orbitals. In the opposite side of the phase diagram, the end member $LaMnO_3$ is orbitally ordered (the orbital degeneracy is lifted) and thus when doping with holes this compound, the orbital degeneracy can be ignored. So, the reasons for the discrepancies between theoretically and experimentally derived phase diagrams is also that often conventional theory neglects the orbital degrees of freedom, the electron-electron interactions and the electron-lattice interaction [158]. Recent theoretical works taking into account the

above ingredients derived the sequence of spin and orbital orders as a function of the hole doping of the type (A-F-A-C-G) [158]or (A-F-A-(C,A)-G) [190].

Monte Carlo simulations [159] also revealed some unexpected results. In fact, the authors found that for some densities of carriers a homogeneous charge distribution was found to be unstable. Further studies, concluded that for an unstable electron density, the ground state is expected to be inhomogeneous [196] with two coexisting phases with different carrier concentration. The different phases were found to be: one AFM containing an excess of carriers (electrons or holes) because for <n>=1or <n>=0 the DE can not take place, while the other is expected to contain the minority carriers (electrons or holes depending on which side of the phase diagram is being studied) and displays FM tendencies.

Electronic phase segregation at small or long scale seems to be a common feature close to particular electronic concentrations in manganites, cuprates [197] and nickelates [198]. In manganites the phase separation (PS) phenomena is expected to happen in the electron rich and hole rich doping levels [159, 196, 199-201].

Macroscopic separation into two phases with different carrier density is difficult due to the long-range Coulomb interaction. For that reason the phase separation phenomena is expected to happen but giving rise to small segregated regions in order to spread the charges more uniformly. The competition between attractive DE interaction, Coulomb repulsion between the carriers and energy associated to lattice distortion determine the size and the shape of the entities resulting from the phase segregation phenomena. Hence, we can expect to have small polarons when one carrier is trapped in the local distortion induced by its presence, droplets, stripes, or macroscopic phase segregation depending on the size of the segregated regions.

In manganite phase diagrams it has been observed that the FM and metallic phases are always surrounded in temperature and carrier density by charge inhomogeneous regions where FM and metallic clusters coexist with insulating and sometimes AFM phases. In this sense, it has been experimentally observed the coexistence of FM and AFM regions in the low doping region of the series of compounds $La_{1-x}Sr_xMnO_3$ [202] [22]. Similarly in the calcium based series, phase separation has been also observed at low dopings by neutron techniques [203] or magnetic resonance techniques [204].

PS has been also observed at other doping levels in manganites. In chapter 7 we have reported evidences of phase separation in the $x\approx1/3$ doping level of the Pr(Ca) family of compounds and it has been also reported in the heavily doped region [205]. In addition, the presence of phase separation into FM polarons in a PM matrix close to T_C was revealed by SANS in x=1/3 doping levels of the La base manganites [41]. Moreover, recent studies based on electron microscopy found the coexistence of CO

domains below T_C coexisting with charge disordered FM domains in certain $(LaPr)_{7/8}Ca_{3/8}MnO_3$ compounds [206].

In the heavily doped regime, there exist some experimental indications of the existence of PS. However, no conclusive evidences existed when we began our study. In this sense, [207] studied some compounds of the $Bi_{1-x}Ca_xMnO_3$ series in the heavily doped region ($x\approx0.8$) and revealed the coexistence of FM and AFM structures. Some optical studies on $x>0.5$ compounds of the same family revealed also signs of PS. (For a review on phase separation see [151]).

Large structures in x>1/2 hole doped systems

Studies on manganite in the heavily hole doped systems have been performed on $La_{1/3}Ca_{2/3}MnO_3$ and $La_{1/4}Ca_{3/4}MnO_3$ [208-211]. In these compounds, large superstructures consistent with an ordering of the e_g electrons in the real space were found. Mori et al. performed a series of studies based on electron microscopy and pointed to the existence of bi-stripe like (Fig. 8-1b) ordering of the charges but neutron and SXRPD (Synchrotron X-Rays powder diffraction) studies revealed that the ordering of the charges was found in these compounds but forming a Wigner crystal (Fig. 8-1a). This ordering of the charges implies that the e_g electrons tend to be as far apart as possible in the real space to minimise the Coulomb repulsion.

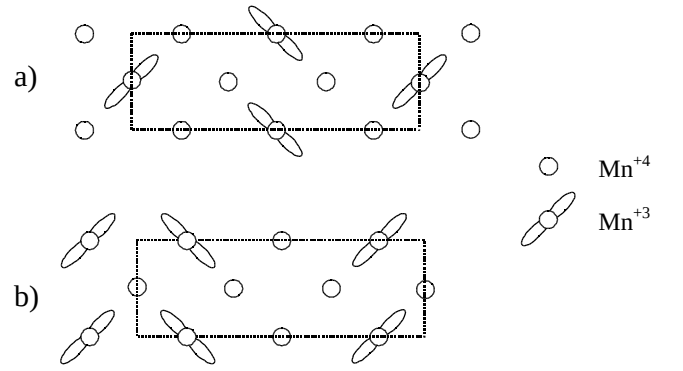

Fig. 8-1 *Schematic projections along the c axis in the Pbnm setting of the proposed a) Wigner cystal and b) stripe like structures of the charge ordered $La_{1/3}Ca_{2/3}MnO_3$ compound*

The discrepancies between the Mn^{+3}/Mn^{+4} arrangement obtained from electron microscopy and neutron and synchrotron diffraction were analysed in [212]. This HREM study concluded that in the $La_{1/3}Ca_{2/3}MnO_3$ compound, the order of the charges was Wigner type. Wang et al. concluded that the HREM images attributed to a bi-stripe arrangement presented by Mori et al. arise from effects related to the HREM technique (thickness or tilting of the specimen, beam defocusing…)

Recently several authors [213-216] [217] began to investigate the heavily hole-doped ($Ln_{1-x}A_xMnO_3$) or electron doped region ($A_{1-y}Ln_yMnO_3$). The findings showing the existence of MR in this hole doped region increased to research in this doping region. A metallic like behaviour with non-saturated ferromagnetic moment has been observed for dopings $x\approx0.88$-0.93 in the $Sm_{1-x}Ca_xMnO_3$

family, which indicates the existence of competing interactions which generate complex magnetic states. Their observations pointed towards a cluster glass metallic state for x<0.1.

The early work of [20] on the $La_{1-x}Ca_xMnO_3$ system displayed a succession of different magnetic, orbital and charge orders in the heavily doped region. The end member $CaMnO_3$ adopts a G-type magnetic structure (T_N≈110K) where each Mn ion is coupled antiferromagnetically to its six near-neighbour manganese ions. For x>0.9 the G type structure of the $CaMnO_3$ compound was observed. In the doping range 0.78>x≥0.5 the CE type AFM structure was reported and for x=0.80 the C type magnetic structure, consisting in FM aligned Mn ions forming FM chains coupled AFM. .

Goodenough went further in the analysis of these structures and predicted that the CE-type structure would be stable in the doping range 0.75>x≥0.5 while the C-type would have 0.9>x≥0.75 [17]. He also pointed out the possibility of PS in the region close to x=0.75 (C-CE type competition) and in the range 0.1>x>0.85 (C-G type competition).

Hence, the study of the highly doped regions presents great attraction due to the presence of several interesting phenomena as charge ordering, orbital ordering, phase separation, magnetoresistance…

Bismuth based manganites

In this chapter, we present the study of the highly hole doped or electron doped phase diagram of the $Bi_{1-x}Ca_xMnO_3$ family.

Bi^{+3}, in contrast to La^{+3} ion, has a highly polarisable $6s^2$ pair and its volume varies depending whether the lone pair character is dominant or not. When the lone pair character is dominant, Bi^{+3} ion has the same volume than La^{+3}. In the other case, the ion is more symmetric and its volume is reduced ($6s^2$ character dominant $<r_{Bi}>^{IX}$≈1.24 Å, $6s^2$ character constrained $<r_{Bi}>^{IX}$≈1.16Å) [218].

Bismuth based manganites behave very different than lanthanum based manganites. The undoped bismuth parent compound, $BiMnO_3$, is FM (T_C≈105K)[219] governed by SE interaction and probably orbitally ordered with a triclinic cell (C2 space group) [220] while the undoped lanthanum compound, $LaMnO_3$, is A type AFM, orbitally ordered with a orthorhombic type cell (Pbnm space group)[156].

The differences between lanthanum based and bismuth based compounds exist also in the parent $LaMnO_3$ and $BiMnO_3$. While the former is AFM insulator, the later is ferromagnetic and ferroelectric. A recent work based on the pseudopotencial calculations using local spin density approximation (LSDA) on those compounds [232], concluded that the main difference between $LaMnO_3$ and $BiMnO_3$ electronic structure is that the latter presents covalent bonding between the Bi cations and the oxygen anions while in the rare earth based manganites the rare earth-oxygen

interaction is essentially purely ionic. Important findings from band calculations is the significant hybridisation between Bi 6p and O 2p orbitals. In this sense, Bi contribution to the charge density was found large and highly directional and the conduction electrons partly occupy p-type atomic orbitals. This contribution of the Bi p-type atomic orbitals is, probably, at the origin of the differences in transport properties between $BiMnO_3$ compound and $LaMnO_3$ because, in the latter, the conduction band is mainly Mn 3d type.

Highly hole doped bismuth based manganite samples are possible to synthesise. Some groups have succeeded on growing single crystals of $Bi_{1-x}Ca_xMnO_3$ with x>1/2 [207] [221]. However, most of the studies have been performed on polycrystalline samples. Early studies on bismuth based manganites date from the 60's [222-226]. Recently, different studies have been performed in the highly hole doped regime [219, 227-229].

Bao et al, [207], studied the charge ordering and the magnetic arrangement on single crystals of $Bi_yCa_{1-y}MnO_3$ for electron doping levels y=0.26,y=0.24 and y=0.18 using elastic an inelastic neutron techniques but they did not give details of the structure. TEM images on x=0.80 compound, [228], displayed the existence of an orbital order which tends to produce the quadrupling of one cell parameter which would be an indication of charge ordering in the C-type structure as predicted by Goodennough [17]. Moreover, on this compound other long period features were reported corresponding to unexpectedly long periodicities of 1/32 and 1/36.

Phase separation phenomena in this heavily doped compounds has been concluded from optical studies on the x=0.76 [229]and x=0.80 [230] $Bi_{1-x}Ca_xMnO_3$ compounds through the identification of two energy ranges in the optical response which show different temperature dependence and can be associated to different physical processes. X-ray studies[221] on a x=0.76 single crystal, agreed with the existence of a charge ordered state with a modulation wave vector δ=0.24, which the authors associated to a stripe like distribution of the Mn ions. However, a Wigner crystal type CO can not be ruled out because the authors only studied the intensities of superlattice peaks and did not give any model which could simulate their experimental results.

Sample preparation

All the bismuth compounds described in the present chapter are ceramic samples obtained by standard solid state ceramic synthesis in air performed at the ICMAB. The starting compounds were Bi_2O_3, $CaCO_3$ and MnO_2. The stoichiometric mixtures were heated at 1000°C several times with intermediate grindings to ensure sample homogeneity and finally in the form of pellets, the samples were annealed at 1250°C during 24h several times. The cooling rates were about 300°C/h. A 4% of Bi_2O_3 in excess was added to the precursors mixture in order to avoid off stoichiometry due to bismuth volatilisation.

Objectives of this study

The main objective of our work has been the study of the effect of bismuth substitution and the understanding of the origin of MR in highly doped compounds, which has been found to be related to macroscopic phase separation phenomena.

In order to study the ground state in the low electron concentration regime and to understand the origin of the observed MR the highly doped regime (x>0.75) we have performed an systematic study on $Bi_{1-x}Ca_xMnO_3$ polycrystalline samples with hole concentration in the interval 0.5<x<0.9. Neutron (ILL) and SXRPD (synchrotron X-Ray) powder diffraction studies in the Debye-Sherrer (transmission) geometry have been undertaken. SXRPD have been collected at BM16 diffractometer at the ESRF (Grenoble) using a double Si (111) crystal monochromator with a selected wavelength of λ=0.442377 Å calibrated with Si NIST.

Transport measurements and magnetoresistance have been performed on ceramic bars with the four-probe method using DC current. Magnetic measurements have been performed using extraction magnetometers up to fields of 10T and in the temperature range between 1.5K-800K at the Laboratory Louis Néel (Grenoble) and at the high magnetic fields laboratory SNCMP (Toulouse).

8.2 Orbital and charge ordering in $Bi_{1/2}Ca_{1/2}MnO_3$ compound

In the following section we will present a comparative study between the bismuth and lanthanum based manganites for the hole doping x=1/2. The objective of this study is to understand the effect of Bi doping in manganites and determining which is the role of the highly polarisable $6s^2$ lone pair in these compounds.

8.2.1 Electrical and magnetic transitions in $Bi_{1/2}Ca_{1/2}MnO_3$ and $La_{1/2}Ca_{1/2}MnO_3$

In addition to the x=1/3 hole doping level, one of the most extensively studied doping levels in lanthanum based manganites has been x=1/2 (for a review [145, 231]). In the present manuscript, we have already presented two compounds of this doping level exhibiting different behaviour at low temperatures. On the one hand, $Pr_{1/2}Sr_{1/2}MnO_3$ (chapter 6) exhibited an A-type AFM order at low temperatures with no sign of charge ordering but exhibiting orbital order. On the other hand, $Pr_{1/2}Ca_{1/2}MnO_3$ has been presented in (chapter 7.2.1) as a paradigmatic example of the x=1/2 charge and orbitally ordered materials.

In Fig. 8-2 is shown the phase diagram for $Ln_{1/2}Ca_{1/2}MnO_3$ compounds as a function of the mean ionic radii at the A-site cation as extracted from [145]. It can be observed that there exist a clear relationship between the ionic radius mismatch at the A-site and the orbital and magnetic ordering temperatures. The origin of the sensitivity of these compounds to the ionic radius mismatch is found to be the increase of the MnO_6 octahedra tilting when $<r_A>$ diminishes. This distortion reduces the Mn-O-Mn bonding angle, while the Mn-O distance remains nearly unchanged. The reduction of the Mn-O-Mn narrows the one electron bandwidth and thus weakens the DE interaction that competes with the carrier-lattice coupling, increasing the charge localisation tendency. Larger octahedra tilting have shown to favour the CO-OO state because it increases the T_{CO} in agreement with the above arguments, but they decrease the AFM ordering temperatures. For larger $<r_A>$ competition between FM and CE-AFM type magnetic structures is evident in Fig. 8-2.

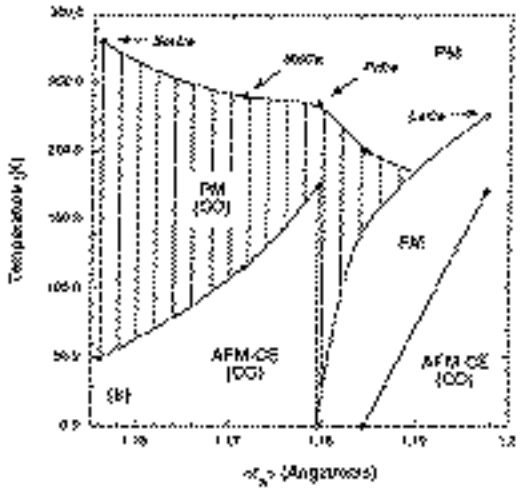

Fig. 8-2 *Phase diagram for $Ln_{1/2}Ca_{1/2}MnO_3$ compounds as a function of $<r_A>$ as extracted from [145]*

An example of the strong competition between DE-FM and SE-AFM interactions can be found in the $La_{1/2}Ca_{1/2}MnO_3$ compound were those states appear successively upon cooling down. At high temperatures $La_{1/2}Ca_{1/2}MnO_3$ is a PM insulator and upon cooling, it firstly becomes FM and metallic (T_C=225K) and then AFM-CO insulator ($T_N \approx$195K). In $La_{1/2}Ca_{1/2}MnO_3$ $T_N \approx T_{CO}$ and the charge-order to charge disorder transition is first order and display hysteresis as extracted from ZF-μSR and dc magnetisation measurements (Fig. 8-3). The analysis of the ZF-μSR has been performed using a stretched exponential function in the region with short range FM order (19K-250K) (Fig. 8-3 and Fig. 8-4). This result contrast with the results obtained for $Pr_{1/2}Ca_{1/2}MnO_3$ (and other RE as Sm and Nd which are not shown in the present manuscript), where the single exponential decay described well the temperature range above the magnetic transition T_N. In $La_{1/2}Ca_{1/2}MnO_3$ the initial asymmetry begins to decrease around 230K due to the existence of static FM coupling and it definitively falls down at $T_{CO}=T_N$.

In Fig. 8-4 is also shown the evolution of the β exponent of the stretched exponential decay function. The onset of $\beta \neq 1$ values is found at about 250K . As mentioned in chapter 7.4.1 the deviation of muon decay from the pure exponential decay function ($\beta \neq 1$) is the signature of the presence of different relaxation rates describing a distribution of local fields or regions due to the formation of FM domains.

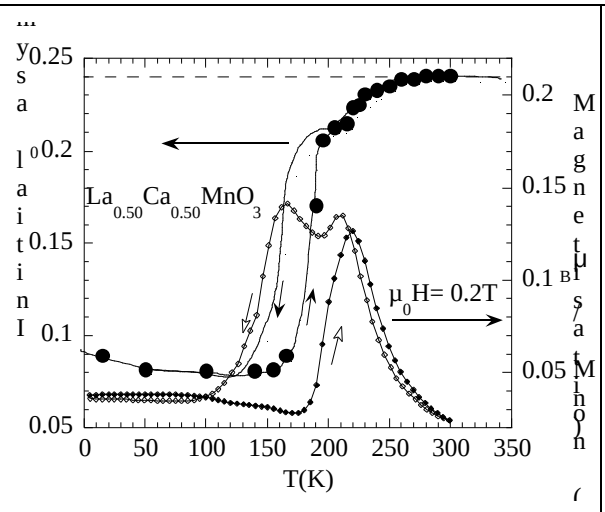

Fig. 8-3 *Thermal hysteresis of the initial asymmetry obtained from ZF-μSR experiments on $La_{1/2}Ca_{1/2}MnO_3$ powder sample and magnetisation measurements under 0.2T*

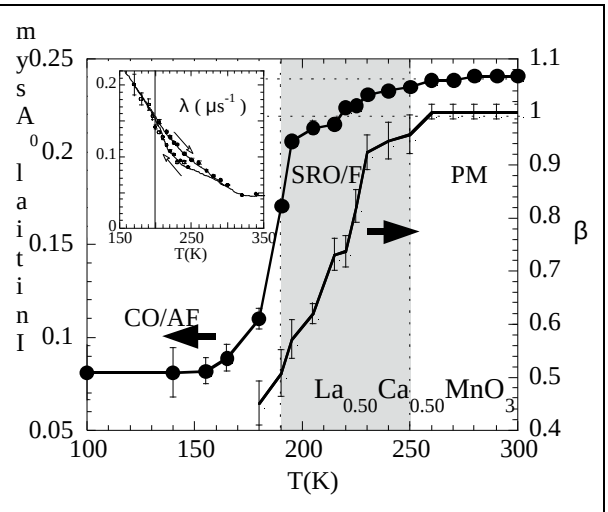

Fig. 8-4 *Thermal evolution of the β exponent and the initial asymmetry upon warming. In the inset, the thermal hysteresis of the relaxation rate is also found.*

Bismuth based manganite with x=1/2 nominal doping exhibit higher CO temperature than the predicted by the bandwidth tuning mechanism in the $Ln_{1/2}(Ca,Sr)_{1/2}MnO_3$ family as shown in Fig. 8-5. The difference between the measured T_{CO} and the predicted from the steric bandwidth narrowing is about 60 K.

Although, Bi^{+3} and La^{+3} have very similar radii in many oxides [218], the replacement of La by Bi in these x=1/2 compounds leads to an decrease of the average Mn-O-Mn of about 5°. Hence, the reasons for those differences should be found in the role that Bi plays in these compounds.

Moreover, Bi ion is more electronegative than rare earths (Pauling electronegativity for Bi≈2.02 and for La and Pr≈1.10-1.13) and than Mn (Pauling electronegativity for Mn≈1.55), hence, this enhances the Bi-O hybridisation and reduces the amount of Mn-O hybridisation.

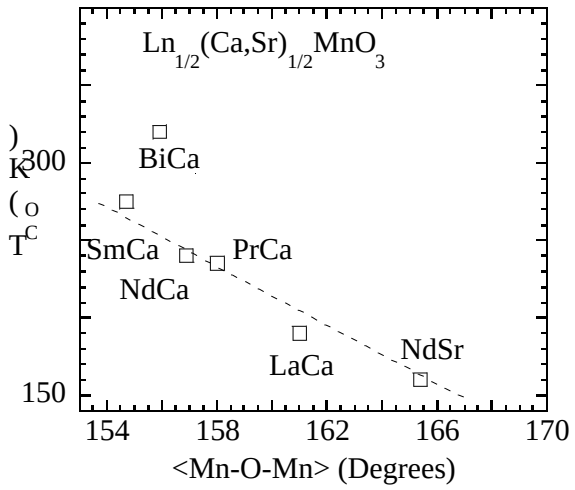

Fig. 8-5 *Dependence of T_{CO} for $Ln_{1/2}(Ca,Sr)_{1/2}MnO_3$ compounds on the mean <Mn-O-Mn> angle.*

8.2.2 Resistivity and magnetisation characterisation of $Bi_{1/2}Ca_{1/2}MnO_3$

We have performed dc resistivity measurements on $Bi_{1/2}Ca_{1/2}MnO_3$ and $La_{1/2}Ca_{1/2}MnO_3$ using the four-probe method on ceramic bars (Fig. 8-6). In contrast with lanthanum based compound, bismuth based sample do not exhibit the metal-insulator transition and it remains insulating up to low temperature. Moreover, the application of a magnetic field of 7T did not appreciably change the resistivity of the sample.

The value of the resistivity at RT is four orders of magnitude smaller than in lanthanum compound and the change on the resistivity observed at T_{CO} and T_N is much less abrupt when compared to most of the half hole doped rare earth based manganites exhibiting CO phenomena.

Magnetisation measurements using a dc extraction magnetometer in the temperature range 1-800K and magnetic fields up to 10T were used to characterise the $Bi_{1/2}Ca_{1/2}MnO_3$ and $La_{1/2}Ca_{1/2}MnO_3$ samples. Magnetic measurements revealed an unexpectedly high T_{CO} in the bismuth based compound.

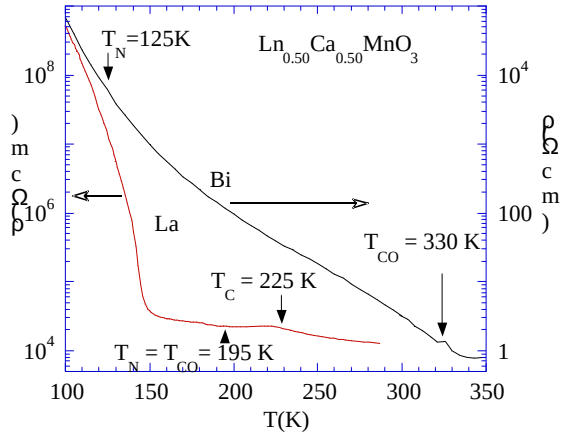

Fig. 8-6 *Resistivity measurements on Lanthanum and Bismuth based $Ln_{1/2}Ca_{1/2}MnO_3$*

In Fig. 8-7 and Fig. 8-8 are shown the magnetisation measurements under an applied field of 1T on the La and Bi based x=1/2 samples. Two features can be observed in the magnetisation curves, the first has been found at 330K and the second feature is observed at 125K in Bi sample which roughly correspond to T_{CO} and T_N respectively while in lanthanum based compound they were found at T_{CO} ≈210K and T_N is ≈155K. In addition, the magnetisation at the T_{CO} transition temperature is largely reduced in bismuth sample when compared to lanthanum sample.

Both samples exhibit a Curie-Weiss behaviour at high temperatures giving θ_P=225K and μ_{eff}=4.38μ_B/Mn in the bismuth based compound and θ_P=257K and μ_{eff}=5.32μ_B/Mn in the lanthanum compound. In both cases, the high temperature magnetic interactions gives a positive θ_p. Hence, at high temperatures the interactions are FM and, in both cases, the effective moments are larger than the theoretical effective moments (3.53μ_B/Mn)

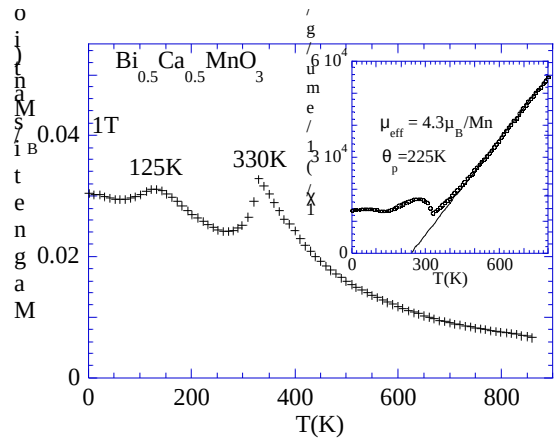

Fig. 8-7 *DC magnetisation measurements under 1T on $Bi_{1/2}Ca_{1/2}MnO_3$ ceramic sample*

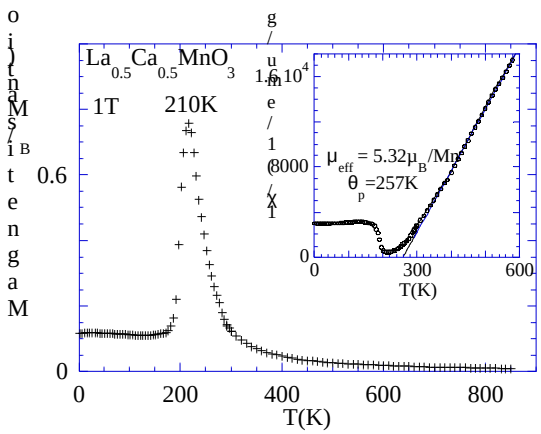

Fig. 8-8 *DC magnetisation measurements under 1T on $La_{1/2}Ca_{1/2}MnO_3$ ceramic sample.*

The thermal evolution of the magnetisation on $Bi_{1/2}Ca_{1/2}MnO_3$ and $La_{1/2}Ca_{1/2}MnO_3$ ceramics under applied magnetic fields up to 10T is shown in Fig. 8-9 and Fig. 8-10. In the lanthanum based sample the application of a magnetic field favours the FM existent between T_C and T_{CO} and the charge ordering temperature shifts towards lower temperatures indicating a smaller strength of the localising tendency in this compound when compared to Bi based compound.

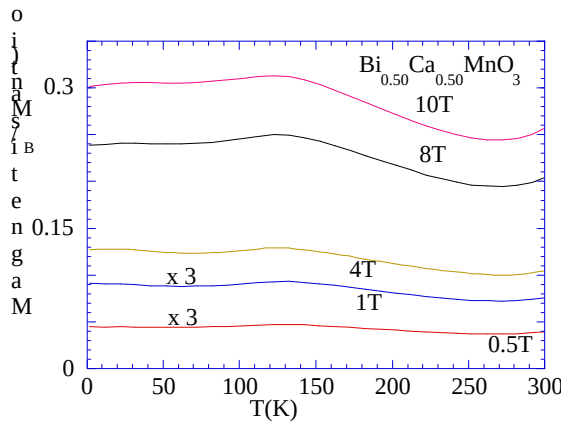

Fig. 8-9 *Thermal evolution of the magnetisation measured with fields up to 10T on $Bi_{1/2}Ca_{1/2}MnO_3$ ceramic samples*

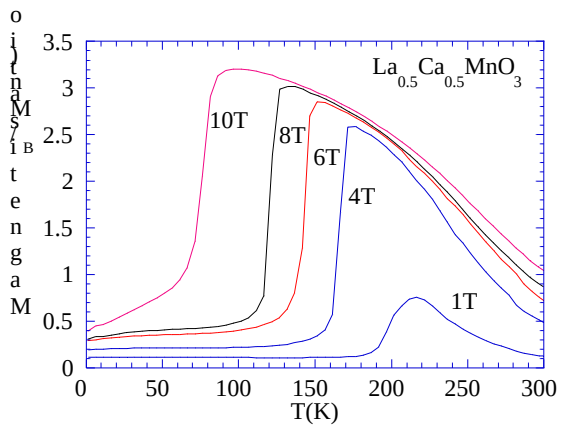

Fig. 8-10 *Thermal evolution of the magnetisation measured with fields up to 10T on $La_{1/2}Ca_{1/2}MnO_3$ ceramic samples*

The stability of the charge ordered state under high magnetic fields has been studied on the light of the results obtained at the SNCMP (Toulouse) with pulsed magnetic fields up to 50T. In Fig. 8-11 and Fig. 8-12 are shown the isothermal evolution of the magnetisation under the application of high pulsed magnetic fields at 4K on both compounds. In the lanthanum based sample, the magnetisation curve displays the melting of the charge ordered state. The magnetisation reached under high magnetic fields corresponds to the fully alignment of Mn ions in lanthanum compound. However, the bismuth based compound is less sensitive to the application of magnetic fields up to 50 Tesla that

are not enough to completely destabilise the ordered state. Nevertheless, is possible to observe a weak change of slope at 40T and small hysteresis is found when comparing the increasing and decreasing sweep field curves. This is an indication of the charge ordering melting in $Bi_{1/2}Ca_{1/2}MnO_3$ compound should begin at 45-50T.

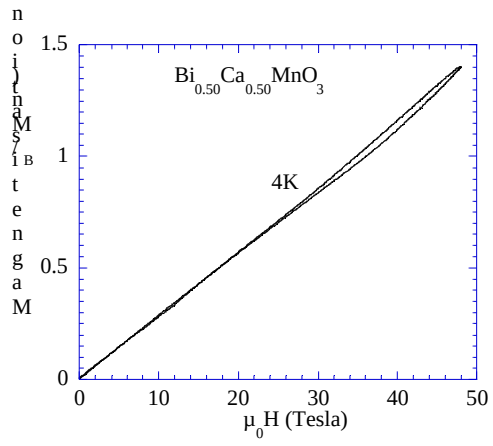

Fig. 8-11 *Isothermal magnetisation versus applied magnetic field curves at 4K on $Bi_{1/2}Ca_{1/2}MnO_3$ and $La_{1/2}Ca_{1/2}MnO_3$ ceramic samples performed at the SNCMP (Toulouse)*

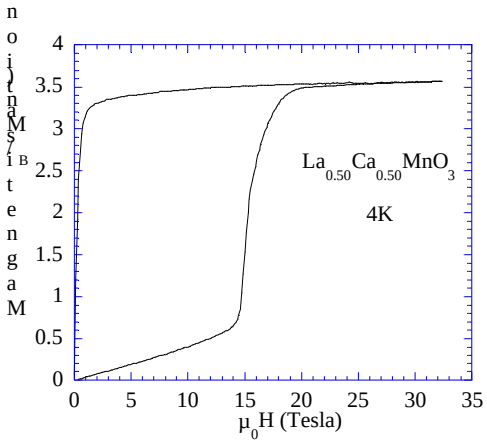

Fig. 8-12 *Isothermal magnetisation versus applied magnetic field curves at 4K on $La_{1/2}Ca_{1/2}MnO_3$ ceramic samples.*

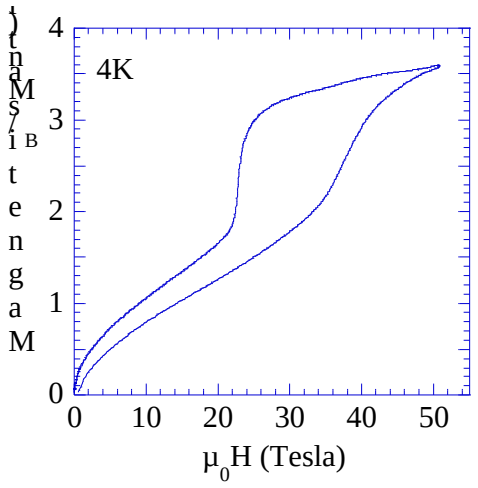

Fig. 8-13 *Magnetisation versus magnetic field curve of $Sm_{1/2}Ca_{1/2}MnO_3$ at 4K*

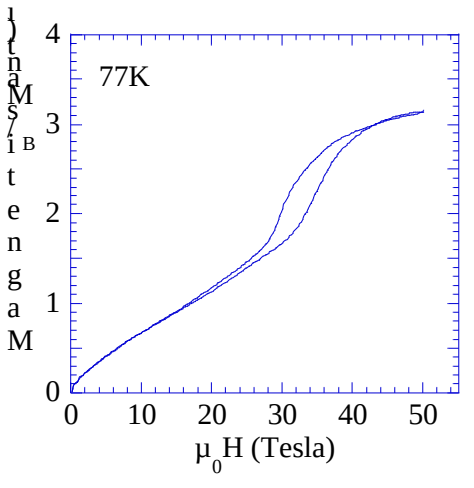

Fig. 8-14 *Magnetisation versus magnetic field curve of $Sm_{1/2}Ca_{1/2}MnO_3$ at 77K*

The stability of the charge ordered state in bismuth based compound could be attributed to the larger bending of the exchange Mn-O-Mn angle when compared to lanthanum compound that we have experimentally determined from NPD data. However, studies on the stability of the charge ordered state under field on the $Sm_{1/2}Ca_{1/2}MnO_3$ (<Mn-O-Mn>=154.7(3)° from [145]) compound, which from the structural point of view is more distorted than $Bi_{1/2}Ca_{1/2}MnO_3$ $_2MnO_3$ (<Mn-O-Mn>=156.1°)

compound, revealed that the critical fields of the more distorted Sm compound are smaller than for the less distorted $Bi_{1/2}Ca_{1/2}MnO_3$ (Fig. 8-13).

From the magnetic measurements we conclude that the charge ordered state is stabilised at higher temperatures in bismuth based compound, and its stability under applied magnetic fields is larger than in the La or Sm based analogue compounds. This stability does not have its origin in a different Mn-O-Mn bonding angle (steric effects). The origin of such high CO stability under field should be attributed to the nature of the bonds of the Bi ions with neighbouring oxygens which changes the conduction band.

8.2.3 Structural transition : A Neutron and synchrotron powder diffraction study

We have performed a series of NPD studies using D20(2.42Å) and D2B(1.594Å) diffractometer in the high intensity mode at ILL in order to characterise the structure and the magnetic order on $Bi_{1/2}Ca_{1/2}MnO_3$ powder sample. D20 diffractometer is a medium resolution instrument which has rather good to study the magnetic structure and allowed to follow the thermal evolution of the cell parameters (2K, 70K, 170K, 300K) and to determine the magnetic structure. D2B instrument has been use for crystallographic structure determination (2K, 300K).

The NPD pattern at 300K of $Bi_{1/2}Ca_{1/2}MnO_3$ sample did not present clear superlattice peaks and was satisfactorily Rietveld refined using the Pbnm space group with a unit cell: a=5.4143(4)Å , b= 5.4624(4)Å and c=7.5197(5)Å . The obtained atom positions are listed in Tab. 8-IV.

One superlattice peak identified in D20 below 170K and it is hardly observed at 300K. It corresponds to the (2 1/2 2) Bragg reflection and appears around 2θ≈68.09°. This superlattice peak was also found in NPD measurements on $La_{1/2}Ca_{1/2}MnO_3$, $Pr_{1/2}Ca_{1/2}MnO_3$ and $Nd_{1/2}Ca_{1/2}MnO_3$ and its apparition is an indication of the existence of a particular orbital ordering which induces a doubling of the unit cell in the *b* direction in the Pbnm setting as discussed in chapter 7.2.1. (structural modulation with

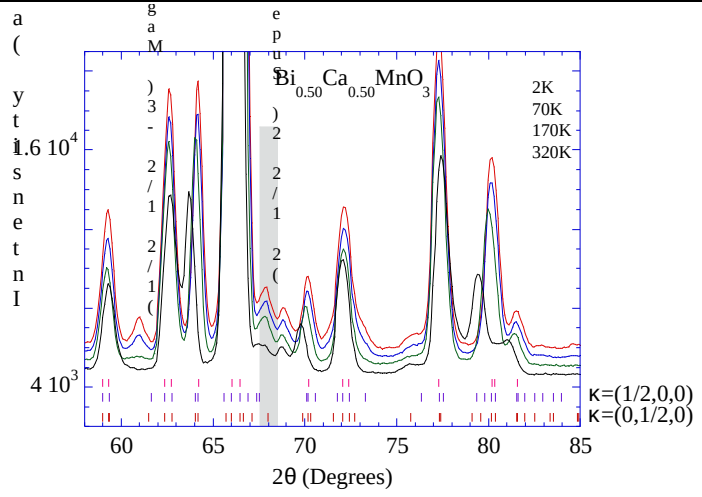

Fig. 8-15 *Selected 2θ range of NPD patterns at different temperatures displaying the apparition of the (2 1/2 2) superlattice peak and one of the CE magnetic peaks.*

κ=(0,1/2,0) wave vector.

The large difference between the *a* and *b* cell parameters permits to rule out the other possible structural modulation vector κ=(1/2,0,0) which was not the case in lanthanum based analogue manganite compound.

In Fig. 8-15 is shown a selected 2θ range of the NPD data obtained at D20 diffractometer where the superlattice peak is observed. In Fig. 8-15 is possible to observe that the superlattice peak appears before the apparition of the AFM peaks (see 170K curve). On the other hand, the thermal evolution of the nuclear peaks shows that below 170K the cell parameters do not seem to appreciably evolve.

Due to the small number of superlattice peaks observed we have described the low temperature structure with the averaged structure using the Pbnm symmetry (a=5.4267(3) Å, b=5.4764Å, c=7.4754(3)Å). In Tab. 8-IV are shown the obtained cell parameters and averaged atom positions from the D2B data refinement at 2K(Fig. 8-16).

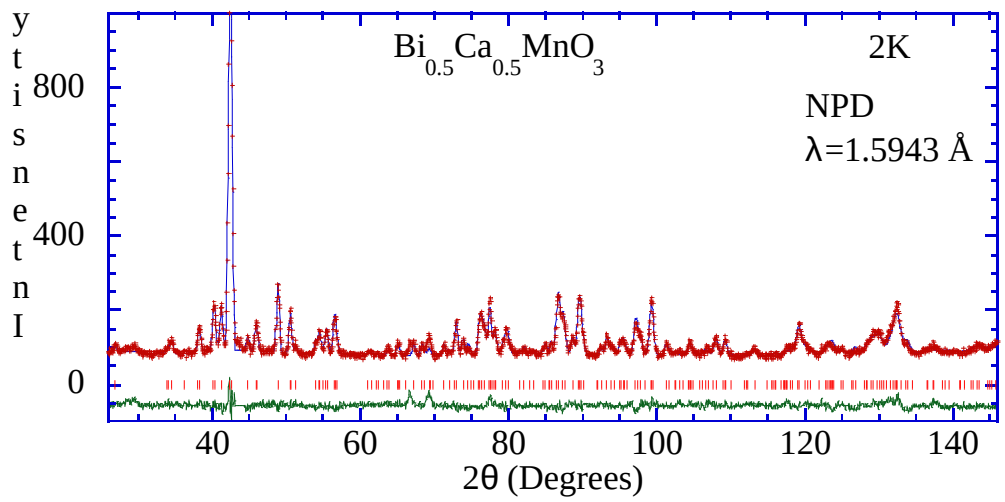

Fig. 8-16 *Refined NPD pattern at 2K (D2B)of* $Bi_{1/2}Ca_{1/2}MnO_3$

In Fig. 8-17 is shown the thermal evolution of the cell parameters as extracted from D2B and D20 NPD refinements and reveals a characteristic anisotropic distortion of the unit cell upon cooling which is found in the x=1/2 hole doped manganites exhibiting the orbital order sketched in Fig. 8-21 and which is usually accompanied at lower temperatures by a CE-type AFM arrangement of the Mn moments. The localisation of the e_g electrons concomitant with the order of the d_z^2 e_g orbitals in the sample describing a zig-zag in the *ab* plane generates the expansion of the *a* and *b* axis and a contraction of the *c* axis as can be observed in the figure Fig. 8-17.

In Tab. 8-I are shown selected calculated distances and angles for $Bi_{1/2}Ca_{1/2}MnO_3$ as obtained from Rietveld refinements of D2B NPD data considering the averaged unit cell. Analogous distances and angles from the lanthanum based compound extracted from [172] are also shown.

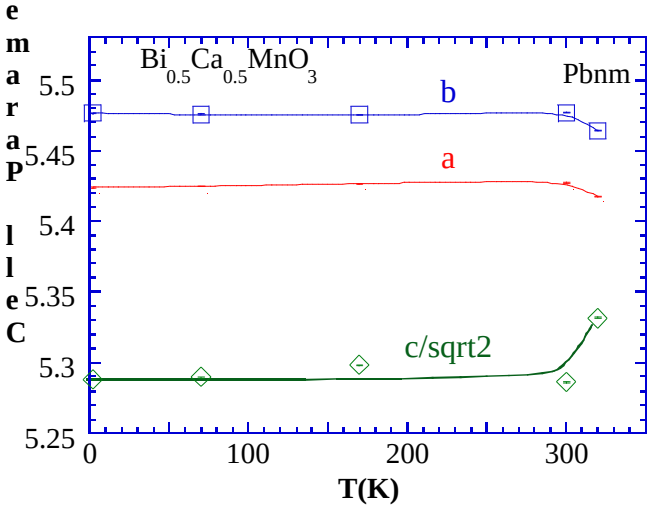

Fig. 8-17 *Thermal evolution of the unit cell parameters for $Bi_{1/2}Ca_{1/2}MnO_3$ from NPD.*

At RT, the $Bi_{1/2}Ca_{1/2}MnO_3$ unit cell is already anisotropically distorted suggesting that the orbital order already exists at RT. This is evidenced by the value of the parameter $\varepsilon_c = \left|1 - \frac{\sqrt{2}c}{a+b}\right| \times 10^3$, which gives an idea of the anisotropic distortion of the unit cell. If the unit cell were cubic ε_c would be 0. At 2K $Bi_{1/2}Ca_{1/2}MnO_3$ gives a value of $\varepsilon_c \approx 30$ while in $La_{1/2}Ca_{1/2}MnO_3$ $\varepsilon_c \approx 23$. At RT, the $La_{1/2}Ca_{1/2}MnO_3$ is not orbitally ordered and thus ε_c is small ≈4, but that is not the case of $Bi_{1/2}Ca_{1/2}MnO_3$ which at RT has $\varepsilon_c \approx 22$.

We have used several parameters to characterise the distortion of the oxygen octahedra. Δ_d, defined as:

$$\Delta_d = \frac{1}{N}\sum_N \left(\frac{d_i - \langle d \rangle}{\langle d \rangle}\right)^2 \qquad \textbf{Eq. 8-1}$$

and ε_d defined as:

$$\varepsilon_d = \left|\frac{d_{equat}}{d_{apic}} - 1\right| \times 10^4 \qquad \textbf{Eq. 8-2}$$

ε_d considers the difference between the apical and equatorial distances. The analysis of the deformations of the octahedra, ε_d, yields to: $\varepsilon_d(2K)=290$, $\varepsilon_d(300K)=197$ for $Bi_{1/2}Ca_{1/2}MnO_3$.The anisotropic distortion of the octahedra is usually associated to the particular orbital order present at this doping level. The calculated values of the two parameters for $Bi_{1/2}Ca_{1/2}MnO_3$ and $La_{1/2}Ca_{1/2}MnO_3$ samples at 2K and RT are given in Tab. 8-I.

The inspection of the Mn-O bond distances in $Bi_{1/2}Ca_{1/2}MnO_3$ and $La_{1/2}Ca_{1/2}MnO_3$ leads us to the conclusion that the octahedra are rather different in bismuth and lanthanum manganites. On the

one hand, the mean Mn-O distance in bismuth compound is larger than in lanthanum compound: 1.951(2) Å versus 1.9428(7).

Moreover, at low temperature, the oxygen octahedra in $Bi_{1/2}Ca_{1/2}MnO_3$ is not homogeneously expanded and, while the Mn-O apical distance is not very different between bismuth and lanthanum compounds (d_{ap}(Bi)=1.9144(8)Å, d_{ap}(La)=1.9148(3)Å), the equatorial Mn-O distance presents a clear expansion in $Bi_{1/2}Ca_{1/2}MnO_3$ respect to $La_{1/2}Ca_{1/2}MnO_3$ (d_{equat}(Bi)=1.970(3), d_{equat}(La)=1.955(1)). Bismuth sample displays an expansion of the equatorial Mn-O distance that is 1.4 times larger than the expansion in the lanthanum sample. In Fig. 8-18 is schematically shown the oxygen octahedra distortion in $Bi_{1/2}Ca_{1/2}MnO_3$.

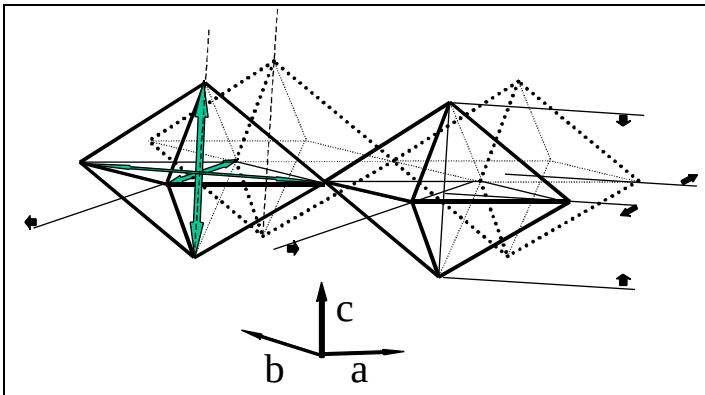

Fig. 8-18 *Schematic figure of the octahedra distortion in the CO state of the $Bi_{1/2}Ca_{1/2}MnO_3$*

Tab. 8-I . *Selected bond distance and angles from high resolution NPD data of $Bi_{1/2}Ca_{1/2}MnO_3$ and of the parent compound $La_{1/2}Ca_{1/2}MnO_3$ as extracted from*[172]

	$Bi_{1/2}Ca_{1/2}MnO_3$		$La_{1/2}Ca_{1/2}MnO_3$	
Parameter	T=2K	T=300K	2K	T=300K
$d_{Mn-O(1)}$ (Å) X 2	**1.9144(8)**	**1.925(1)**	***1.9148(3)***	***1.9406(3)***
$d_{Mn-O(2)}$ (Å) X 2	1.969(3) 1.972(3)	1.966(3) 1.961(3)	*1.951(1)* *1.959(1)*	*1.944(2)* *1.946(2)*
$d_{equat (Å)}$	**1.970(3)**	**1.963(3)**	***1.955(1)***	***1.945(2)***
$<d_{Mn-O}>$(Å)	**1.952(2)**	**1.951(2)**	***1.9416(7)***	***1.9428(7)***
$\Delta_d \times 10^4$	1.83	0.87	*0.98*	*0.01*
$\varepsilon_d = \left\| \frac{d_{equat}}{d_{apic}} - 1 \right\| \times 10^4$	**290**	**197**	*209*	*22*
Bi (La) / Ca – O(1) (Å) X 1	3.117(5) 2.432(5) 3.082(5)	3.091(6) 2.441(6) 3.091(6)	*2.904(2)* *2.593(2)* *3.076(2)*	*2.881(3)* *2.591(2)* *3.026(2)*
Bi (La) / Ca - O(2) (Å) X 2	2.389(5) 2.557(3) 2.376(3) 2.651(3) 3.241(3)	2.364(6) 2.573(4) 2.398(4) 2.646(4) 3.224(4)	*2.410(2)* *2.592(1)* *2.728(1)* *3.061(1)* *2.442(2)*	*2.417(2)* *2.633(2)* *2.716(1)* *3.085(1)* *2.443(2)*
<Bi (La)-O> Å	2.722(3)	2.722(4)	*2.719(1)*	*2.722(1)*
Mn - O(1) - Mn (deg)	154.95(3)	155.16(4)	*158.51(8)*	*160.23(9)*
Mn - O(2) - Mn (deg)	155.9(1)	156.6(1)	*161.93(5)*	*161.65(6)*
<Mn - O – Mn> (deg)	**155.58(7)**	**156.1(1)**	*160.79(6)*	*161.18(7)*

In Tab. 8-II are shown selected bond distances and angles at RT for the $Ln_{1/2}Ca_{1/2}MnO_3$ (Sm, Bi, Nd and La) compounds. The inspection of the Mn-O angles reveals that at RT the octahedra in bismuth compound exhibits the larger Mn-O bond mean distance which is mainly due to the existing

expansion of the octahedra in the basal planeThe MnO_6 octahedra are expanded in $Bi_{1/2}Ca_{1/2}MnO_3$ with respect to any of the other $Ln_{1/2}Ca_{1/2}MnO_3$ compounds.

Tab. 8-II *Selected bond distance and angles of the $Ln_{1/2}Ca_{1/2}MnO_3$ family of compounds at RT*

	$Sm_{1/2}Ca_{1/2}MnO_3$ from [145]	$Bi_{1/2}Ca_{1/2}MnO_3$	$Nd_{1/2}Ca_{1/2}MnO_3$ from [145]	$La_{1/2}Ca_{1/2}MnO_3$ from [172]
Parameter	T=300K	T=300K	T=300K	T=300K
$d_{Mn-O(1)}$ (Å) X 2	***1.933(1)***	**1.925(1)**	***1.936(2)***	***1.9406(3)***
$d_{Mn-O(2)}$ (Å) X 2	*1.956(5)* *1.949(6)*	1.966(3) 1.961(3)	*1.957(6)* *1.925(6)*	*1.944(2)* *1.946(2)*
$d_{equat (Å)}$	***1.952(6)***	**1.963(3)**	***1.941(6)***	***1.945(2)***
$<d_{Mn-O}>$(Å)	***1.946(3)***	**1.951(2)**	***1.939(5)***	***1.9428(7)***
Δ_d	***0.24***	**0.88**	***0.45***	***0.01***
$\varepsilon_d=\left\lvert \frac{d_{equat}}{d_{apic}}-1 \right\rvert \times 10^4$	*100*	197	*25*	*22*
Mn - O(1) - Mn (deg)	*154.9*	155.16(4)	*157.2(4)*	*160.23(9)*
Mn - O(2) - Mn (deg)	*154.6*	156.6(1)	*157.5(2)*	*161.65(6)*
<Mn - O – Mn> (deg)	***155.9***	**156.1(1)**	***157.4(3)***	***161.18(7)***

From inspection of the Mn-O-Mn bonding angles (Fig. 8-19) it is inferred that the ionic radii of Bi^{+3} in this compounds is $<r_{Bi}^{+3}>^{IX}$=1.16Å instead 1.24Å, which would be expected if the $6s^2$ lone pair character were dominant. When the lone pair character is constrained, the $6s^2$ orbitals tend to point towards far from the Bi-O bonds. When the lone pair character is dominant, the $6s^2$ lone pair is weakly screened and presumably the electron density of the lone pair is highly along some Bi-O, bonds producing a larger effective Bi^{+3} ionic size.

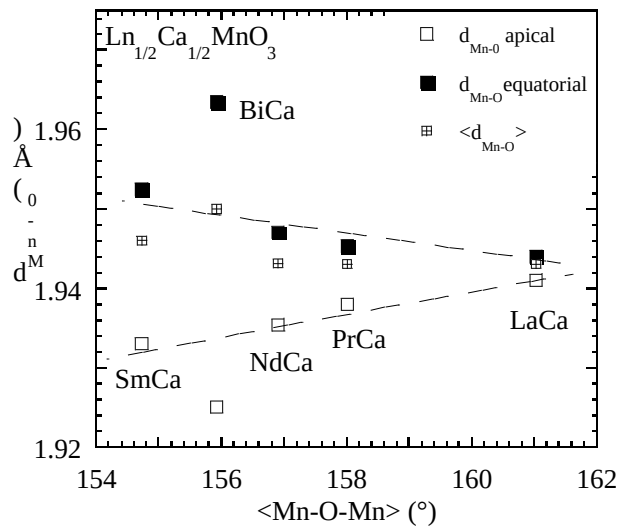

Fig. 8-19 *Mn-O distances and <Mn-O-Mn> angles in the series of compounds $Ln_{1/2}Ca_{1/2}MnO_3$ at RT.*

8.2.4 Magnetic structure of $Bi_{1/2}Ca_{1/2}MnO_3$

The magnetic structure at low temperatures has been identified as the CE-type as described by [20]. An averaged Pbnm unit cell description was used and the magnetic cell was found to be 2ax2bxc.

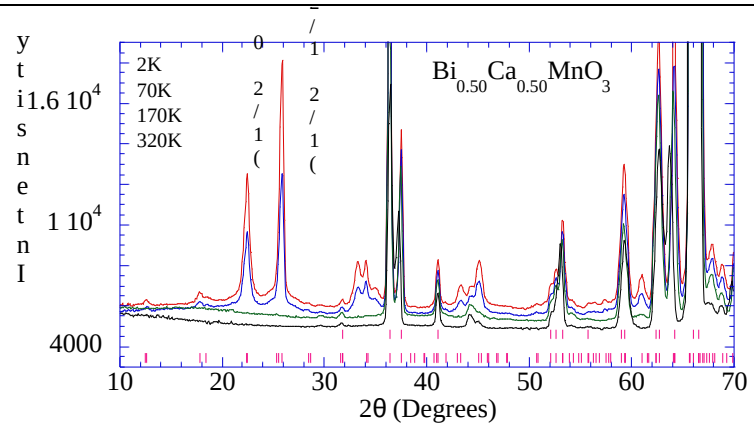

Fig. 8-20 *Selected 2θ range of the NPD patterns in the range were the most intense AFM peaks appear.*

The evolution of the magnetic peaks is shown in a selected 2θ range of the D20 NPD patterns (Fig. 8-20). The refined low angle NPD pattern is shown in Fig. 8-21. A schematic image of the magnetic order observed in this sample is shown in Fig. 8-22. An additional coupling in the *c* direction was added to account for the existence of intensity in the (1/2 00) and (1/2 1/2 0) magnetic reflections

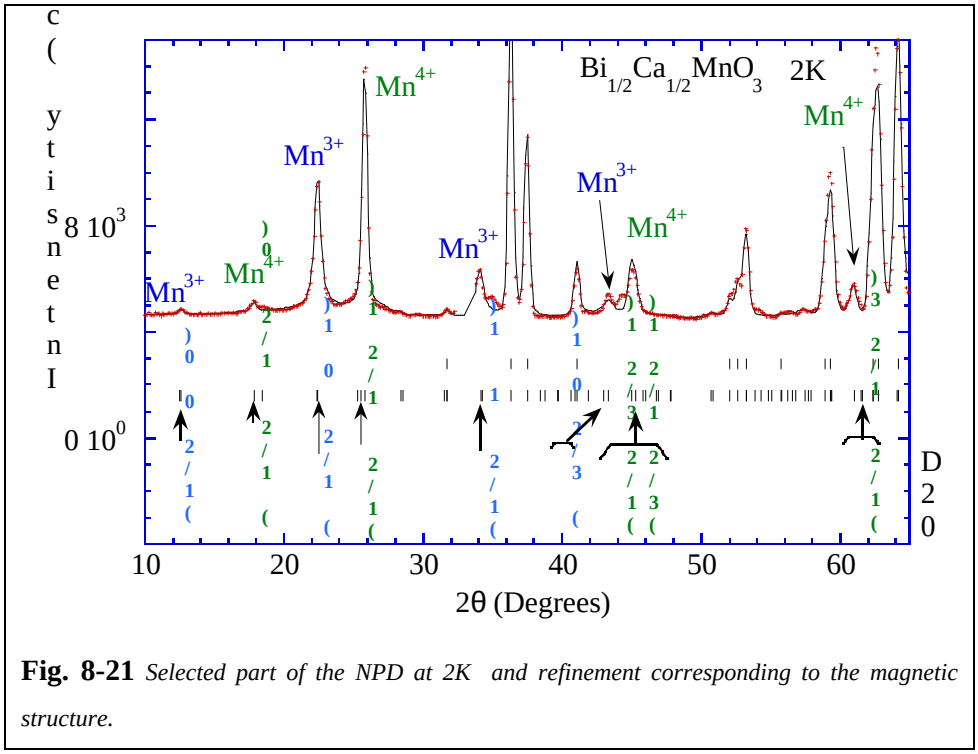

Fig. 8-21 *Selected part of the NPD at 2K and refinement corresponding to the magnetic structure.*

of the 2a×2b×c located at 2θ<20°. Tab. 8-III displays the magnetic moments found in this compound at 2K.

Two slightly different Mn moments have been found which could be associated to Mn^{+3} and Mn^{+4} ions and the obtained moments are 2.6(2) and 2.9(2)μ_B/Mn. However, while the obtained magnetic moment for the Mn^{+4} is close to the theoretical, the magnetic moment associated to Mn^{+3} ion is smaller than the expected value. The magnetic moments are mainly in the *ab* plane and only a small component is found of that plane (≈0.3 or 0.4μ_B/Mn in Mn^{+3} and Mn^{+4}). When the moments were constrained to be in the *ab* plane, the obtained values were Mn^{+3}=2.7μ_B/Mn and Mn^{+4}=2.4μ_B/Mn and a non collinear magnetic structure was obtained. However, we have observed a difference in the FWHM in the magnetic peaks associated to different Mn ion that is consistent with what has been reported in the literature for $La_{1/2}Ca_{1/2}MnO_3$. The magnetic peaks associated to Mn^{+3} ion are more broadened and lorentzian than those associated to Mn^{+4} ion as shown in Fig. 8-21. The estimated coherence length for Mn^{+4} magnetic order is about 4000Å while it is only 800 Å for Mn^{+3} suggesting the presence of antiphase domains in the Mn^{+3} magnetic order.

Tab. 8-III *Results of the magnetic refinement of the NPD data on $Bi_{1/2}Ca_{1/2}MnO_3$ ($R_{mag\,F}$=7)*

Mn^{+3}= 2.6(2)		Mn^{+4}=2.9 (2)	
Site	(2.0(1),1.6(1),0.33(7))μ_B/Mn	Site	(2.3(2),1.7(1),0.40(5))μ_B/Mn
(1/4,0,0)	+1 +1 +1	(0,1/4,0)	+1 +1 +1
(3/4,0,0)	-1 -1 -1	(1/2,1/4,0)	-1 -1 -1
(1/4,1/2,0)	+1 +1 +1	(0,3/4,0)	-1 -1 -1
(3/4,1/2,0)	-1 -1 -1	(1/2,3/4,0)	+1 +1 +1
(1/4,0,1/2)	-1 -1 +1	(0,1/4,1/2)	-1 -1 +1
(3/4,0,1/2)	+1 +1 -1	(1/2,1/4,1/2)	+1 +1 -1
(1/4,1/2,1/2)	-1 -1 +1	(0,3/4,1/2)	+1 +1 -1
(3/4,1/2,1/2)	+1 +1 -1	(1/2,3/4,1/2)	-1 -1 +1

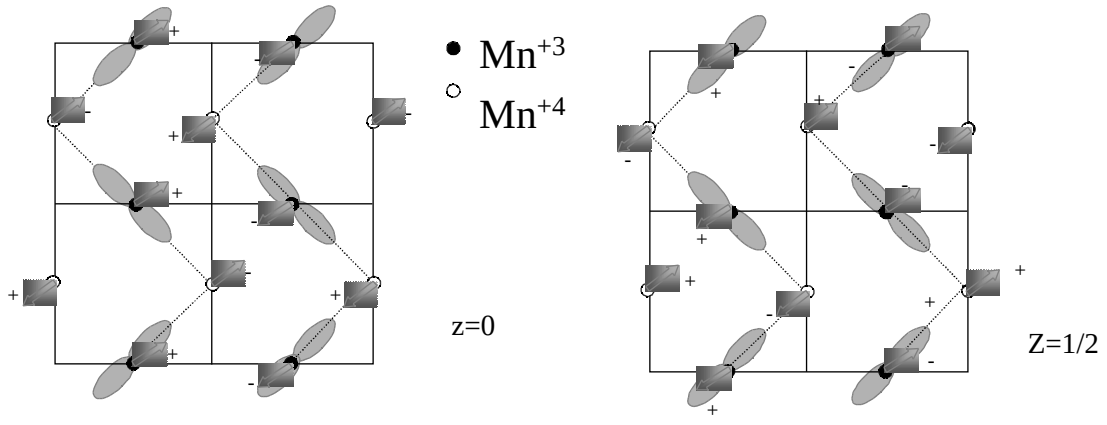

Fig. 8-22 *Schematic image of the magnetic order at low temperature in $Bi_{1/2}Ca_{1/2}MnO_3$*

Tab. 8-IV *Refined structural parameters from high resolution NPD data of $Bi_{1/2}Ca_{1/2}MnO_3$ and cell parameters of the parent compound $La_{1/2}Ca_{1/2}MnO_3$ as extracted from*[172]

		$Bi_{1/2}Ca_{1/2}MnO_3$		$La_{1/2}Ca_{1/2}MnO_3$	
Temperature		2K	RT	*2K*	*RT*
Parameter		Pbnm	Pbnm	*Pbnm*	*Pbnm*
a (Å)		5.4267(3)	5.4143(4)	*5.4763(3)*	*5.4355(1)*
b (Å)		5.4764(3)	5.4624(4)	*5.4466(3)*	*5.4248(1)*
c (Å)		7.4754(3)	7.5197(5)	*7.5247(4)*	*7.6470(2)*
ε_c		30.3	22.3	*25.7*	*4.2*
V $(Å)^2$		222.16(2)	222.39 (2)	*224.44(2)*	*225.485(9)*
Bi(La)/Ca	x	-0.0089(6)	-0.0063(8)	*0.4964(2)*	*0.4952(4)*
	y	0.0417(6)	0.0414(7)	*0.0194(3)*	*0.0195(3)*
	z	0.25	0.25	*0.25*	*0.25*
		0.69(5)	1.02(6)		
Mn1	x	0.5	0.5	0.5	0.5
	y	0	0	0	0
	z	0	0	0	0
		1.00(9)	0.75(9)		
O1	x	0.0733(6)	0.0740(8)	*0.5645(2)*	*0.5608(3)*
	y	0.4783(7)	0.4811(8)	*0.4905(4)*	*0.4926(4)*
	z	0.25	0.25	*0.25*	*0.25*
		0.64(5)	1.00(7)		
O2	x	0.7127(6)	0.7139(7)	*0.2271(2)*	*0.2236(2)*
	y	0.2862(5)	0.2860(6)	*0.2720(2)*	*0.2763(2)*
	z	0.0398(3)	0.0380(3)	*0.0337(1)*	*0.0307(1)*
		1.29(6)	1.36(6)		
χ^2		2.13	1.38		
Ordered Moment		2.7(1)		*2.97(5)*	
(μ_B/Mn)		2.48(9)		*2.57(2)*	
R_{wp} (%)		7.07	6.72	*5.85*	*4.54*
Rf-factor		8.94	8.13	*9.46*	*3.69*

8.2.5 Conclusions

In conclusion, based on NPD, magnetisation, and transport data, we have presented a study of the CO compounds $Bi_{1/2}Ca_{1/2}MnO_3$ which reveals that the CO in bismuth compound develops above room temperature (T_{CO}=330K). The analysis of our NPD data suggests that the lone pair character of the $6s^2$ bismuth orbitals is not dominant in calcium compounds. The <Mn-O-Mn> bonding angle is found to be 156.1° at RT which is slightly less distorted than Sm based compound (<Mn-O-Mn>=155.9°) but more distorted than Nd based compound (<Mn-O-Mn>=157.4°). That means that the effective ionic radius of bismuth is closer to Sm than to La ($6s^2$ lone pair is not dominant). Nevertheless, the CO transition temperature for $Bi_{1/2}Ca_{1/2}MnO_3$ is about 60K above the predicted temperature from steric bandwidth narrowing law.

A comparative study of the CO stability under field between the bismuth and the analogous lanthanum and samarium based compounds has been performed and revealed that the CO is more stable in the bismuth compound. The origin of the high stability of the CO state has been frequently associated to the bandwidth tuning mechanism which works well for most of the $RE_{1/2}(Ca,Sr)_{1/2}MnO_3$ compounds but it fails to explain the behaviour of the bismuth based manganites.

We found experimentally that the MnO_6 octahedra is unexpectedly expanded with respect to other compounds of the x=1/2 series (Fig. 8-19). A large expansion takes place in the basal Mn-O distances (1.15% respect to d_{equat} of Sm compound) and a contraction in the Mn-O apical distances (-0.41% respect $d_{Mn-O(1)}$ of Sm compound) giving rise to a mean distance increase of about 0.26% respect Sm compound.

The effective mean Mn-O bond distance has been found larger than in other x=1/2 compounds and it can be the cause of the reduction of the DE interaction in Bi compound, leading to an unexpected increase of the stability under field of the CO and to a higher T_{CO}.

The origin of the highly anisotropic distortion of the MnO_6 octahedra is still lacking. However, in the non doped compound ($BiMnO_3$) the O 2p and Bi 6p orbital hybridisation seems to be the cause of FM. So we can not rule out in the case of x=1/2 a possible electronic origin of the anisotropic MnO_6 octahedra distortion and the longer <Mn-O> bonding distances.

8.3 Coexistence of quasi -degenerated ground states in $Bi_{1/3}Ca_{2/3}MnO_3$

In this section, we present a study of the orbital and magnetic ordering in the $Bi_{1/3}Ca_{2/3}MnO_3$ compound. The coexistence of several orbital orders at low temperature has been evidenced indicating that the low temperature state is quasi-degenerated. The observation and analysis of different structural modulations associated to orbital ordering has been possible using high resolution SXRPD data because, conversely with $La_{1/3}Ca_{2/3}MnO_3$ for instance, the *a* and *b* lattice parameters are very different in $Bi_{1/3}Ca_{2/3}MnO_3$.

A comparative study is presented between our results on $Bi_{1/3}Ca_{2/3}MnO_3$ and those reported on $La_{1/3}Ca_{2/3}MnO_3$ compound. The magnetic order at low temperature is also investigated using NPD data and results in a similar magnetic structure as the one reported for lanthanum based compound.

8.3.1 Introduction: Wigner versus bi-stripe configurations

In manganites, there is a strong interplay between the charge, spin, phononic and orbital degrees of freedom and the ground state at a certain doping level should minimise the total energy of the system. In x=2/3 compounds if the elastic energy were predominant, when the charge localisation

takes place, the Mn^{+3} ions would tend to be placed as close as possible in order to minimise the lattice distortion associated to the $Mn^{+3}O_6$ octahedra, thus reducing the elastic energy of the system (bi-stripe model). But the Mn^{+3} would tend to be as far apart as possible if Coulomb energy have to be minimised (Wigner-crystal)

Studies based on electron diffraction and transmission electron microscopy at low temperatures evidenced the presence of superlattice reflections, which were attributed to large charge ordered structures in highly hole doped manganites, with a modulation wave vector following the relationship: $\kappa=(0,1-x,0)$ where x is the hole concentration [208, 211]. For $La_{1/3}Ca_{2/3}MnO_3$ compound was reported a superlattice consisting in a tripled simple cell along one of the in-plane axes (*a* or *b* axis in the Pbnm setting). From these electron diffraction studies, the authors claimed the presence of stable pairs of $Mn^{+3}O_6$ octahedra separated periodically by stripes of non distorted $Mn^{+4}O_6$ octahedra (bi-stripes).

Latter on, neutron powder diffraction studies disagreeded with these results, supporting a model for the same compound characterised by the stacking of Mn^{+3} rows situated as far apart as possible in the *ab* plane in order to minimise the Coulomb repulsion energy (Wigner crystal) [210] [209]. Finally, Wang and co workers confirmed the Wigner Crystal model using electron diffraction and electron microscopy demonstrating the previous misinterpretation of the high resolution electron imaging in precedent works was due to optical effects arising from a short list of causes [212].

Theoretical studies based on the Hartree-Fock approximation considering the doubly degeneracy of e_g orbitals, on site Coulomb repulsion and nearest neighbour interaction, concluded that Wigner crystal model should be the ground state. In addition, the bi-striped model could be the ground state at the surface of the crystal because of the smaller elastic constant on the surface [233]. The Wigner crystal model and bi-stripe models are schematically sketched in Fig. 8-1.

Two works have been published trying to address the magnetic and structural order of the $La_{1/3}Ca_{2/3}MnO_3$ compound from NPD and SXRPD [209, 210]. These works propose the Wigner crystal model as the ground state at this hole doping concentration but disagree in the direction of the structural modulation. Fernandez Diaz et al. found $\kappa=(1/3,0,0)$ and Radaelli et al. claimed that a better agreement was found when the $\kappa=(0,1/3,0)$ modulation vector is considered (both referred to the Pbnm setting). The ambiguity in the structural modulation vector in lanthanum based compound appears due to the similar *a* and *b* cell parameters. However, in bismuth based compound, the *a* and *b* cell parameters are rather different and using high resolution SXRPD we have been able to observe the coexistence of several domains with different structural modulations.

In the following section we will present the resistivity and magnetisation characterisations on $Bi_{1/3}Ca_{2/3}MnO_3$ polycrystalline sample.

8.3.2 Resistivity and magnetisation characterisation

The thermal evolution of the resistivity measured using the four-probe method and without field and under applied magnetic field on $Bi_{1/3}Ca_{2/3}MnO_3$ bars of sintered ceramics is shown in Fig. 8-23. The kink in the resistivity at T≈300K corresponds to the onset of the orbital ordering where thermal hysteresis is observed. Below T_{CO}≈300K the resistivity increases several orders of magnitude upon cooling.

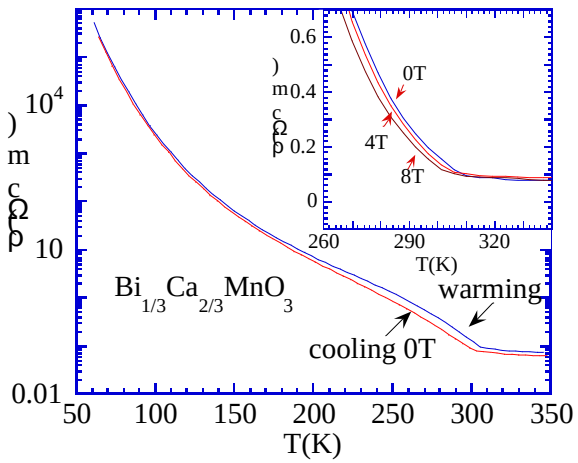

Fig. 8-23 *Resistivity measurements at zero applied field warming and cooling down. In the inset is shown the effect of the application of magnetic fields up to 8T.*

The AFM transition is hardly observed, but a change of slope at T_N≈125K marks a change towards a more resistive state that can be associated to the onset of the AFM phase. The application of magnetic fields up to 8T slightly reduces the resistivity at T_{CO} but the effect is small, about -20% at 300K under 8T of applied magnetic field.

Magnetisation measurements have been performed using an extraction magnetometer up to magnetic fields of 10T in the temperature range 1.5K-800K on polycrystalline samples. $Bi_{1/3}Ca_{2/3}MnO_3$ exhibits a drop in the magnetisation curves that can be associated to the orbital ordering transition at T_{CO}=300 K (Fig. 8-24). The second feature in the magnetisation curve of $Bi_{1/3}Ca_{2/3}MnO_3$ occurs around 125 K and corresponds to T_N in agreement with resistivity data. No evidence of CO melting has been observed in magnetic fields up to 10T.

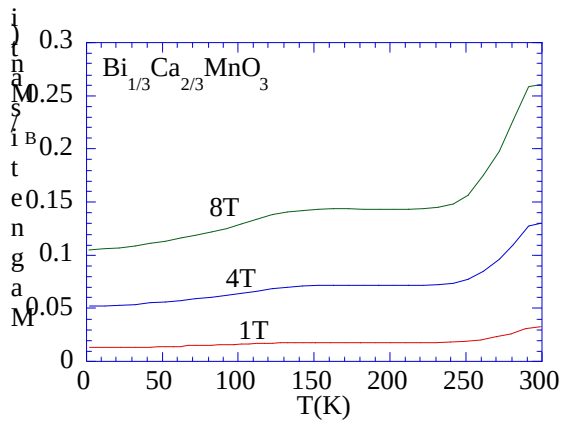

Fig. 8-24 *Thermal evolution of the magnetisation under different applied magnetic fields in $Bi_{1/3}Ca_{2/3}MnO_3$ polycrystalline sample*

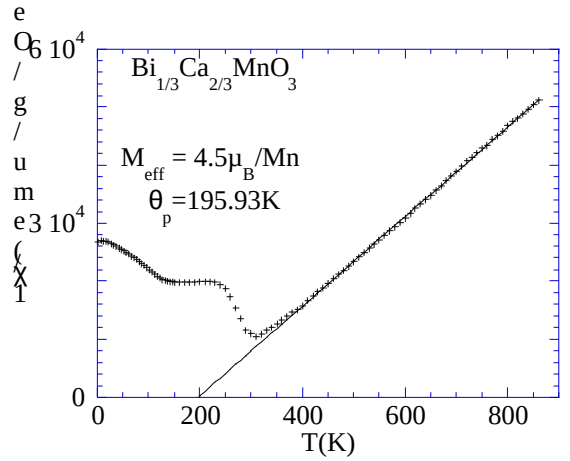

Fig. 8-25 *Inverse of the dc susceptibility measurd under 1T of applied magnetic field on $Bi_{1/3}Ca_{2/3}MnO_3$*

Dc susceptibility measurements (Fig. 8-25) under 1T and up to 800K showed a Curie Weiss law with a positive θ_P=193K and an effective paramagnetic moment (4.5μ_B/Mn), which is larger than the expected moment (3.36μ_B/Mn) and is the largest found for the $Bi_{1-x}Ca_xMnO_3$ family of samples with x>1/2, as shown in Fig. 8-26.

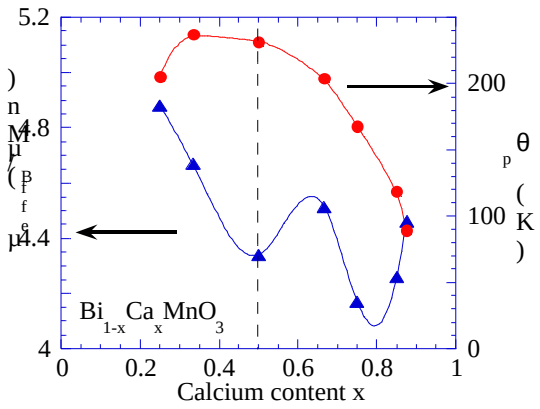

Fig. 8-26 *Evolution of the effective paramagnetic moment from DC susceptibility measurements under 1T of applied magnetic field.*

8.3.3 Structure of $Bi_{1/3}Ca_{2/3}MnO_3$: A neutron and synchrotron study

The study of lattice distortions at the transition temperatures presented in this section has been carried out using ultra-high resolution synchrotron diffraction (SXRPD) data collected on BM16 powder diffractometer of ESRF (Grenoble-France) in Debye-Scherrer (transmission) configuration at selected temperatures (10K-250K-400K). The polycrystalline sample was loaded in a borosilicate glass capillary (φ=0.5mm) and rotated during the data collection. A short wavelength of 0.442377(2) Å was selected with a double Si (111) monochromator. In addition NPD patterns were also collected on D2B (λ=1.594Å) powder diffractometer in the high intensity flux mode at the ILL (Grenoble-France) at 2K, 170K and 300K.

Rietveld refinements were performed using FULPPROF software. When NPD and SXRPD patterns were collected at the similar temperatures, joint refinements were performed refining simultaneously neutron and synchrotron X-Rays powder diffraction data.

At 400K, far above T_{CO}, the sample is well described with an orthorhombic Pbnm structure (a=5.35139(2)Å, b=5.38634(2)Å, c=7.56556(3)Å R_p=6.13%). Additional small spurious peaks were identified by SXRPD as belonging to an impurity identified as $CaMn_2O_4$ (1.3% in volume). The MnO_6 octahedra is found not to be much distorted at 400K. In addition, the apical Mn-O-Mn bonding angle is rather bent, 154.7°, in contrast with the Mn-O-Mn equatorial bonding angle which is 156.8°. Atomic positions and selected distances are listed in Tab. 8-IX and Tab. 8-VI.

Upon cooling through T_{CO}, a set of extra peaks are observed, which are not indexed with the Pbnm unit cell given above. The extra peaks have been identified as superlattice peaks and their study will be presented in the following section.

Joint refinements of NPD and SXRPD data were performed at low temperature (2K-NPD and 10K-SXRPD) and at high temperature (300K). In order to account for the temperature difference of the patterns, neutron wavelength was also refined. In Fig. 8-27 are shown the observed and calculated patterns obtained from joint Rietveld refinement of SXRPD and NPD data considering the averaged Pbnm described above. The patterns display good agreement. Selected distances and bonds obtained from those refinements on $Bi_{1/3}Ca_{2/3}MnO_3$ compound and for $La_{1/3}Ca_{2/3}MnO_3$ (extracted from [209]) are listed in Tab. 8-VI.

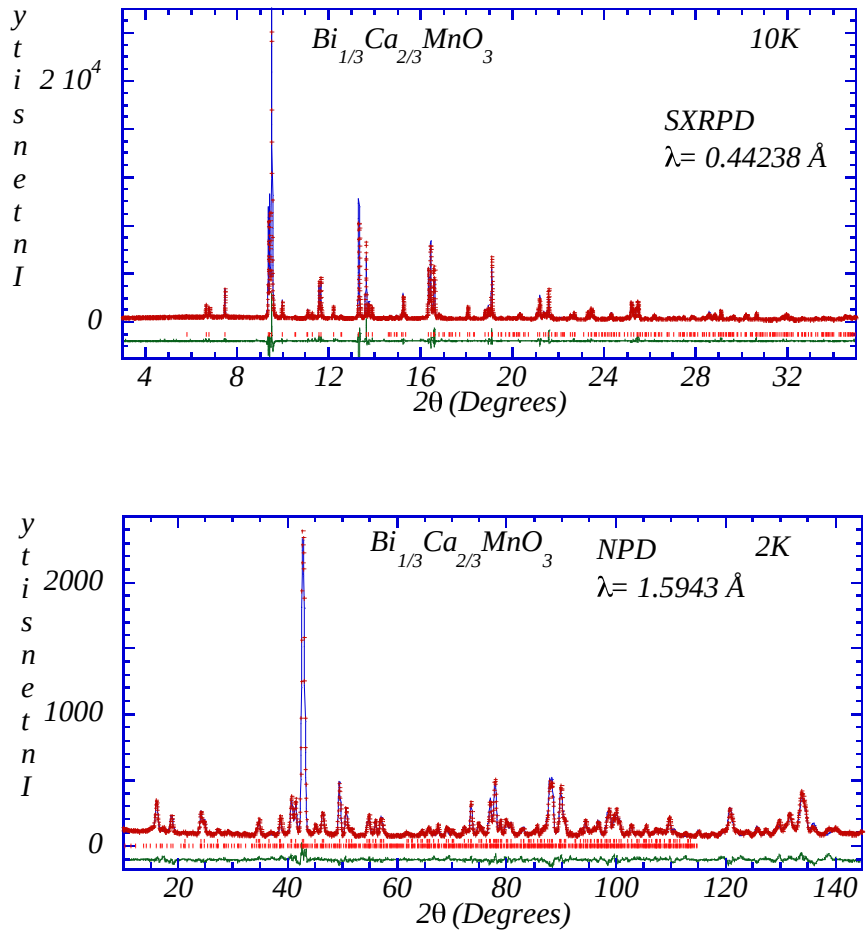

Fig. 8-27 *Rietveld plot of $Bi_{1/3}Ca_{2/3}MnO_3$ SXRPD and NPD data at low temperature (10K-2K respectively) from joint refinement.*

From the NPD and SXRPD patterns and using an averaged Pbnm structure, the thermal evolution of the averaged cell parameters was determined (Fig. 8-28). The cell parameters of the averaged unit cell of $Bi_{1/3}Ca_{2/3}MnO_3$ compound display an anisotropic thermal evolution below T_{CO} which can be associated to the stabilisation of orbital ordering. Upon cooling there is a reduction of the

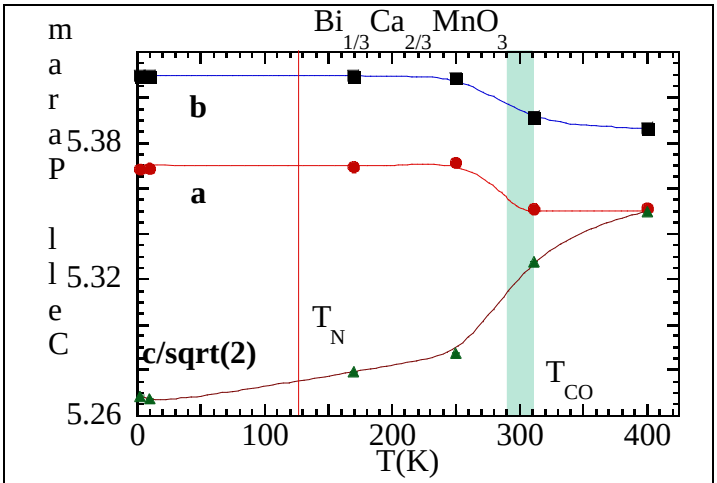

Fig. 8-28 *Temperature dependence of the averaged unit cell parameters for $Bi_{1/3}Ca_{2/3}MnO_3$.*

c cell parameter (Pbnm setting) and an expansion of the *ab* plane which recalls the thermal evolution presented by x=1/2 CO compounds which presented a d_{z^2} orbital ordering in the *ab* plane.

Inspection of the averaged cell parameters below T_{CO} reveals that, in contrast to the similar *a* and *b* cell parameters of the parent $La_{1/3}Ca_{2/3}MnO_3$ compound reported in [209, 210], $Bi_{1/3}Ca_{2/3}MnO_3$ exhibits larger differences between the *a* and *b* cell parameters (see the value of $\frac{2(a-b)}{(a+b)}*10^2$ parameter in Tab. 8-V) and the anisotropic unit cell distortion parameter (ε_c) is comparatively larger in $Bi_{1/3}Ca_{2/3}MnO_3$ than in $La_{1/3}Ca_{2/3}MnO_3$ for similar temperatures.

The difference in the cell parameters is very positive when determining or distinguishing structural modulation vectors, as we will do in the following section. Moreover, it makes previous determination of propagation vectors rather questionable because the similarities of *a* and *b*.

Tab. 8-V: *Comparison between the $Bi_{1/3}Ca_{2/3}MnO_3$ (BiCa) averaged cell parameters determined from Rietveld NPD and SXRPD refinement and $La_{1/3}Ca_{2/3}MnO_3$ (LaCa) averaged cell parameters extracted from* [209]

	10K-BiCa	170K-BiCa	*160K-LaCa*	250K-BiCa	311K-BiCa	*300K-LaCa*	400K-BiCa
a(Å)	5.36899(5)	5.3694(2)	*5.4081(1)*	5.37227(2)	5.3508(1)	*5.3864(1)*	5.35139(2)
b(Å)	5.40991(5)	5.4095(2)	*5.3962(1)*	5.40924(2)	5.3913(1)	*5.3812(1)*	5.38634(2)
c(Å)	7.44955 (6)	7.4660(3)	*7.4988(1)*	7.47854(3)	7.5345(2)	*7.5687(1)*	7.56556(3)
$\varepsilon_c = \left(1 - \frac{\sqrt{2}c}{a+b}\right)\times 10^3$	22.6	20.4	*18.4*	19.0	8	*5.9*	3
$\frac{2(a-b)}{(a+b)}*10^2$	-0.75	-0.74	*0.22*	-0.68	-0.75	*0.10*	-0.65

From inspection of the determined bonds distances and angles (Tab. 8-VI), the <Mn-O> distance is found to be larger in x=2/3 bismuth based manganite, similarly to the x=1/2 case. Moreover, in this case the equatorial distance is also unexpectedly expanded while the apical distance is rather comparable to lanthanum compound. The degree of anisotropic distortion of the octahedra is reflected by ε_d which is 214 in the bismuth compound at 175K while is only 149 in the lanthanum compound at the similar temperature. In addition, the dispersion of the Mn-O bonding distances is also larger in bismuth based compound Δ_d(Bica-175K)=1.54 while Δ_d(LaCa-165K)=0.50.

In Fig. 8-29 is shown the thermal evolution of Mn-O bond distances. Upon cooling below T_{CO}, the octahedra become more anisotropic, undergoing a shortening of the apical Mn-O distance (-1.6%) and an expansion of the equatorial or basal Mn-O (0.41%) distance. This anisotropic distortion does change the volume of the MnO_6 octahedra by 1% while in lanthanum based compounds the volume of the octahedra do not meaningfully change upon cooling through T_{CO} (Fig. 8-30). This fact is suggesting that additional phenomena may contribute to the octahedra distortion in bismuth system.

The large octahedra volume change upon cooling through the charge ordering transition temperature has never been reported before. For well characterised x=1/2 lanthanum based samples the volume contraction upon cooling is about -0.3% which is found to be within the error as extracted from [172].

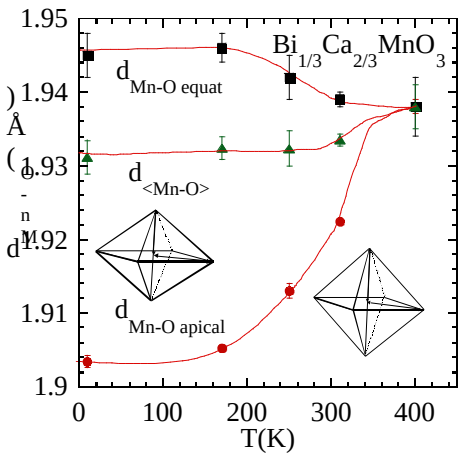

Fig. 8-29 *Obtained Mn-O distances from NPD and SXRPD Rietveld refinements on $Bi_{1/3}Ca_{2/3}MnO_3$*

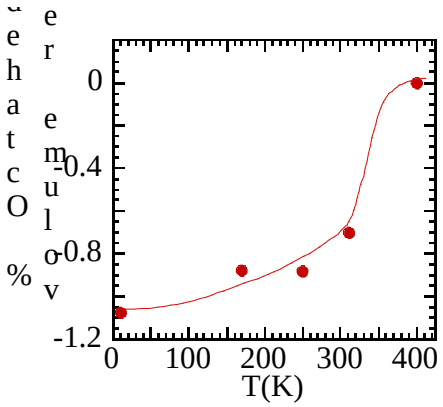

Fig. 8-30 *Thermal evolution of the calculated oxygen octahedron volume in $Bi_{1/3}Ca_{2/3}MnO_3$*

On the other hand, it is important to notice that, upon cooling, the Mn-O-Mn apical bonding angle opens and it approaches the value of the Mn-O-Mn equatorial-bonding angle contrarily to what happens in lanthanum based compound. In the lanthanum compound upon cooling the apical bond angle becomes more distorted (Mn-O(1)-Mn (300K)=160.6(1)°, Mn-O(1)-Mn (165K)=159.05(9)°).

In order to get further insight on the low temperature structure and to identify the AFM ordering appearing below 125K we have performed a detailed study of the extra peaks which were not indexed using a $\sqrt{2}a_p \times \sqrt{2}a_p \times 2a_p$ unit cell.

Tab. 8-VI *Selected bond distances and angles for $Bi_{1/3}Ca_{2/3}MnO_3$ extracted from the Rietveld refinement of NPD and SXRPD data (BiCa). Data for $La_{1/3}Ca_{2/3}MnO_3$ is from* [209] *(averaged unit cell).*

	T=10K SXR-NPD T=2K	T=175K NPD	*T=165K LaCa*	T=250K SXRPD	T=311K SXR-NPD	*T=300K LaCa*	T=400K SXRPD
	Pbnm	Pbnm		Pbnm	Pbnm		Pbnm
$d_{Mn-O(1)}$ (Å) X 2	**1.9034(8)**	**1.9052(5)**	***1.9065(3)***	**1.913(1)**	**1.9224(4)**	***1.9196(3)***	**1.938(1)**
$d_{Mn-O(2)}$ (Å) X 2	1.957(3)	1.952(2)	*1.938(2)*	1.947(5)	1.943(1)	*1.936(2)*	1.942(4)
	1.933(3)	1.939(2)	*1.932(2)*	1.938(5)	1.935(1)	*1.923(5)*	1.933(4)
d_{equat} (Å)	**1.945(3)**	**1.946(2)**	***1.935(2)***	**1.942(3)**	**1.939(1)**	***1.929(4)***	**1.938(4)**
$<d_{Mn-O}>$ (Å)	**1.931(2)**	**1.932(1)**	***1.925(1)***	**1.932(5)**	**1.933(1)**	***1.926(2)***	**1.938(3)**
ε_d	218	214	*149*	151	86	*48*	0
Δ_d	1.28	1.54	*0.50*	0.55	0.19	*0.13*	0.03
Bi / Ca - O(1) (Å) X 1	3.042(4)	3.035(3)		3.035(6)	3.006(2)		2.993(4)
	2.437(4)	2.437(3)		2.443(6)	2.443(2)		2.467(4)
	3.035(4)	3.033(3)		3.065(6)	3.046(3)		3.080(6)
	2.369(4)	2.371(3)		2.341(6)	2.336(3)		2.299(6)
Bi / Ca - O(2) (Å) X 2	2.536(3)	2.551(2)		2.559(5)	2.589(2)		2.618(4)
	2.372(3)	2.374(2)		2.395(5)	2.381(2)		2.384(4)
	2.637(3)	2.629(2)		2.628(5)	2.626(2)		2.609(4)
	3.192(3)	3.196(2)		3.172(5)	3.183(2)		3.184(4)
<Bi-O> Å	2.696	2.698		2.699	2.699		2.702
Mn - O(1) -Mn (°)	156.18(3)	156.86(2)	*159.05(9)*	155.40(5)	156.93(2)	*160.6(1)*	154.73(5)
Mn - O(2) -Mn (°)	156.9(1)	156.68(8)	*161.48(5)*	157.8(2)	156.60(6)	*161.13(6)*	156.8(2)
<Mn-O-Mn> (°)	**156.66(6)**	**156.74(5)**	***160.67(7)***	**157.0(1)**	**156.71(4)**	***160.95(8)***	**156.1(1)**
R_{wp}(%)	9.27(X) 8.85(N)	7.90		10.50	6.40		9.30
R_p(%)	6.86(X) 6.69(N)	5.77		8.40	4.98		6.13
Bragg R-factor	5.86	7.69		7.32	6.79		3.70

8.3.3.1 Orbital ordering

At low temperature, the SXRPD patterns display a series of extra peaks that were absent above the charge ordering temperature, T_{CO}≈300K (Fig. 8-31). The most intense of these peaks is about 1% the intensity of the most intense nuclear peak. In the following section we will identify these peaks as coming from the structural modulation originated by the orbital ordering.

In Fig. 8-31 are shown the extra peaks found in the SXRPD data at 10K. The 400K pattern is also displayed for comparison. Careful examination of the superlattice peaks, suggests that there exist four sets of lattice modulations: κ_1=(1/3, 0, 0), κ_2=(0,1/3,0), κ_3=(1/3, 1/2, 0) and κ_4=(1/2, 1/3, 0). In Fig. 8-31 we have shown with the rows the Bragg reflections corresponding to these structural modulation vectors below each superlattice peak.

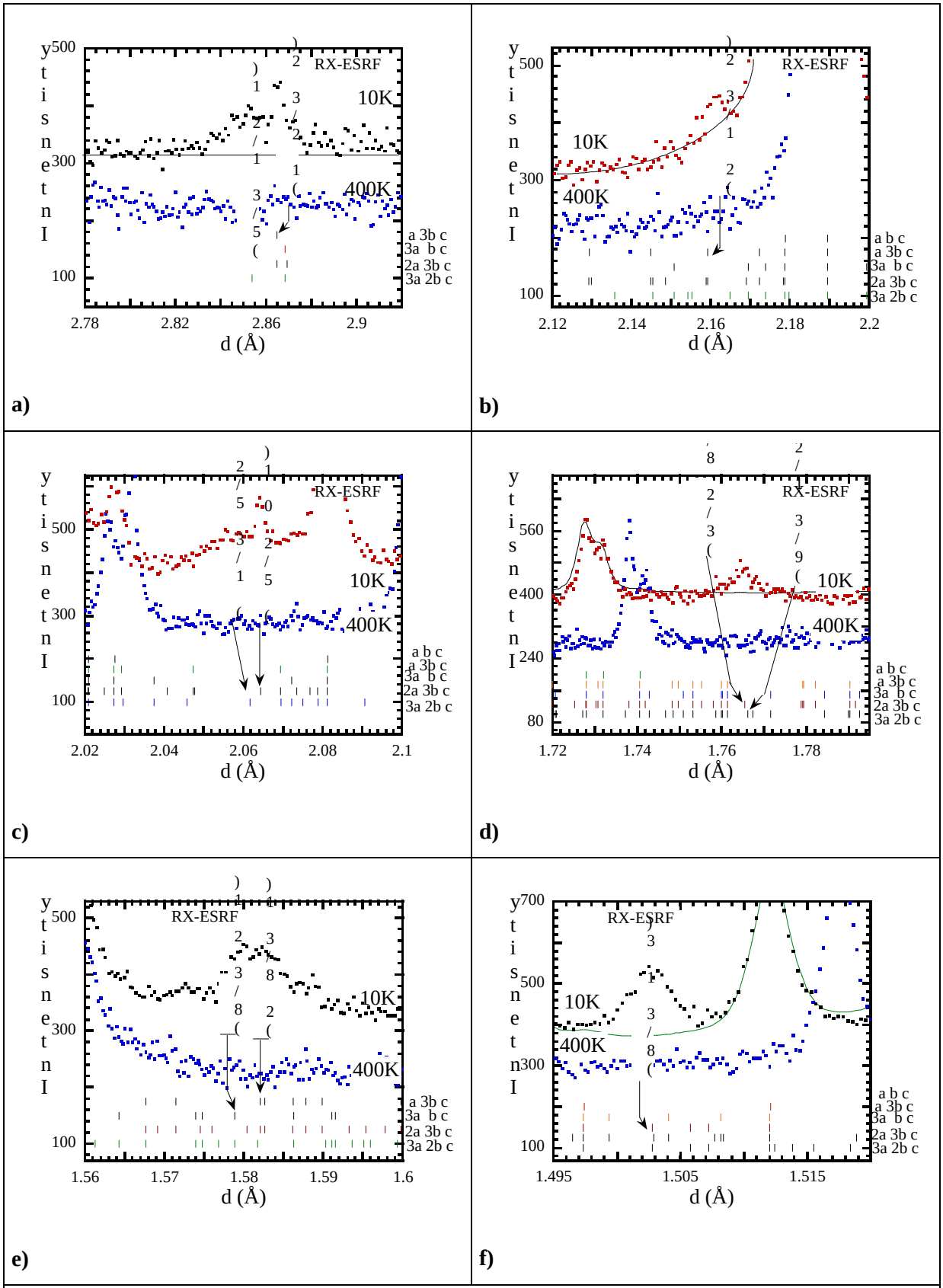

Fig. 8-31 *Superlattice peaks appearing on SXRPD patterns below T_{CO} referred to the averaged Pbnm cell parameters*

Our results clearly show that the structural modulations reported up to now for $La_{1/3}Ca_{2/3}MnO_3$, corresponding κ_1 and κ_2, are not the only structural modulations. Clear evidences are the existence of the (3/2 8/3 0) and (9/3 1/2 0) (Fig. 8-31 d)) and of (1/3 5/2 1) and (5/2 0 1) (Fig. 8-31 c)) superlattice peaks. In addition, we could not find any superlattice peak unambiguously associated to κ_1 or κ_2 structural modulation vectors. For example, at low temperature we have noticed the a superlattice peak which could be identified as (8/3 1 3) (Fig. 8-31 d)) associated to κ_1 but also to (8/3 2/2 3) or (7/2 0 1) corresponding to κ_3 and κ_4 respectively. Similarly, we found intensity at the (8/3 2 1) position (Fig. 8-31 e)) corresponding to κ_1 but it could also be identified as (8/3 4/2 1) corresponding to κ_3. A summary of the identification of the superlattice peaks, their position and normalised integrated intensity respect to the more intense peak as well as their FWHM is shown in Tab. 8-VII. For simplicity, we have indexed the superstructure peaks with the smallest possible cell.

Tab. 8-VII *Position and integrated intensity of the superlattice peaks observed in $Bi_{1/3}Ca_{2/3}MnO_3$ sample from SXRPD patterns. The indexation of the peaks is also proposed on the basis of the averaged Pbnm averaged cell parameters.*

2θ (Degrees)	d(Å)	Integ. Int.	Norm I.I× 10^{-3}	2πk(Å^{-1}) ×10^{-3}	κ_1 (1/3,0,0)	κ_2 (0,1/3,0)	κ_3 (1/3,1/2,0)	κ_4 (1/2,1/3,0)
16.929	1.502	6.0(6)	**4.5(6)**	1.6(2)	**(8/3 1 3)**		(8/3 2/2 3)	(7/2 0 1)
16.102	1.579	2.1(2)	1.6(2)	1.2(4)	**(8/3 2 1)**		(8/3 4/2 1)	
16.072	1.582	2.0(2)	1.5(2)	1.9(3)		**(2 8/3 1)**	(3/3 3/2 4)	(4/2 8/3 1)
14.400	1.765	4.0(3)	**3.0(3)**	1.6(1)			(9/3 1/2 0)	**(3/2 8/3 0)**
12.351	2.056	1.5(2)	1.1(2)	*2.5(7)*			**(1/3 5/2 1)**	
12.303	2.064	2.5(5)	**2.9(5)**	**0.5(1)**				**(5/2 0 1)**
11.748	2.162	1.5(4)	1.1(4)	1.1(6)		**(2 1/3 2)**		*(4/2 1/3 2)*
8.901	2.850	2.9(6)	**2.2(6)**	*2.4(5)*			**(5/3 1/2 1)**	
8.854	2.865	1.7(2)	1.3(2)	**0.5(1)**		(1 2/3 2)		**(2/2 2/3 2)**

Superlattice peak width analysis (using Eq. 7-1) reveals that the domains with κ_4=(1/2,1/3,0) structural modulation have the largest coherence length ((2πk)≈0.0005 Å^{-1} with ξ=1/k) which has been estimated to be ξ≈2000 Å (Fig. 8-33). In addition, domains with κ_2 structural modulation display a coherence length of about ξ≈800 Å, which is larger than the obtained for domains with κ_3 structural modulation. The latter are found to be ξ≈400Å. The smaller domains are found to be the ones associated to κ_3 structural modulation ((2πk)≈0.0025 Å^{-1}). The estimated domain size for κ_3 structural modulation is about 400 Å (see (5/3 1/2 1) and (1/3 5/2 1) peaks).

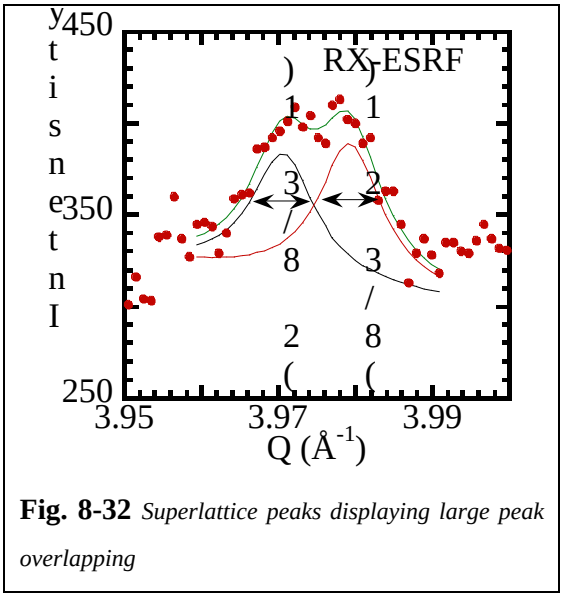

Fig. 8-32 *Superlattice peaks displaying large peak overlapping*

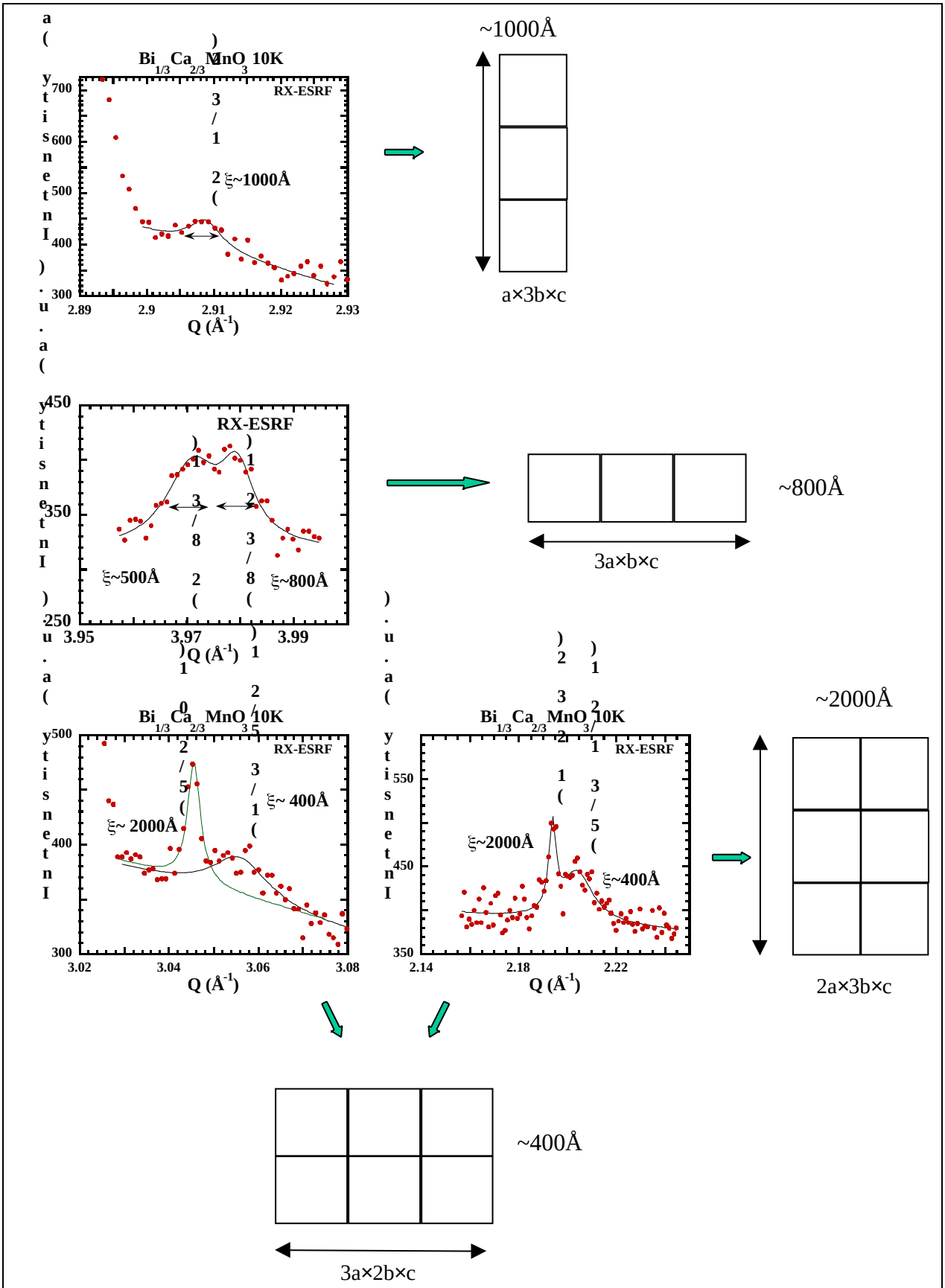

Fig. 8-33 *Estimation of the coherence length of the different superstructures detected in $Bi_{1/3}Ca_{2/3}MnO_3$ by SXRPD measurements at 10K.*

The analysis of the superlattice peaks integrated intensity is difficult to perform due to peak overlapping (Fig. 8-32). The determination of the integrated intensity of the superlattice peaks is the clue to determine the proportion of each of the phases. The superlattice peak with larger integrated intensity can be identified as the (8/3 1 3) but it could also correspond to (8/3 2/2 3) or (7/2 0 1) (Fig. 8-31 f)). Its peak width is large compared to the peak width associated to κ_4 structural modulation and narrow when compared to the peak width associated to κ_3. Thus, indicating that it has contributions from domains with different structural modulations.

This leads us to conclude that the domains with two component larger structural modulations (κ_3, κ_4) are the majority phases (see (5/2 0 1) and (3/2 8/3 0) peaks). However, the coherence length of κ_4 structural modulation is five times larger than in κ_3. Thus, the majority phase probably corresponds to a structural modulation of the type (1/2,1/3,0) which has never been reported before.

The majority structural modulation was not unambiguously determined when using SXRPD data alone. For that reason, further analysis was required using high-resolution NPD data on the same sample. The analysis of the NPD data revealed the existence of four peaks present at 2K and 175K that were not present in the 310K NPD pattern (Fig. 8-34) and that were identified as superlattice peaks (Tab. 8-VIII).

Tab. 8-VIII *Position superlattice peaks observed in $Bi_{1/3}Ca_{2/3}MnO_3$ sample from NPD patterns. The indexation of the peaks is proposed on the basis of the averaged Pbnm averaged cell parameters.*

2θ (Degrees)	κ_1 (1/3,0,0)	κ_2 (0,1/3,0)	κ_3 (1/3,1/2,0)	κ_4 (1/2,1/3,0)
69.53	(7/3 1 4)	(0 4/3 5)	(7/3 2/2 4)	(0 4/3 5)
91.64	(10/3 2 4)		(10/3 4/2 4)	(9/2 3/3 2)
112.59		(5 4/3 3)		(7/2 2/3 6) (5/2 15/3 1) (10/2 4/3 3)
138.82	(7/3 3 7)	(5 4/3 5)	…	…

The peak observed at 138° was too large and its indexation with larger cells was clearly ambiguous, for that reason we only have indexed on the basis of the cells obtained from κ_1 and κ_2 structural modulations.

Inspection of the superlattice peaks found in NPD (Fig. 8-34) data suggests that κ_4=(1/2,1/3,0) structural modulation should be the majority phase for several reasons:

a) All the superlattice peaks found in the NPD pattern could be indexed on the basis of the large unit cell given by κ_4

b) Two of the superlattice peaks could not be indexed when using the other superlattices and where clearly better described considering the cell given by κ_4 structural modulation (see Fig. 8-34b) c))

c) Due to the lower number of counts in NPD pattern, if κ_4 were not majority it would be rather difficult to find its associated superlattice peaks in NPD patterns.

These results agree with the results of the study of the superlattice peaks on this compound obtained by SXRPD.

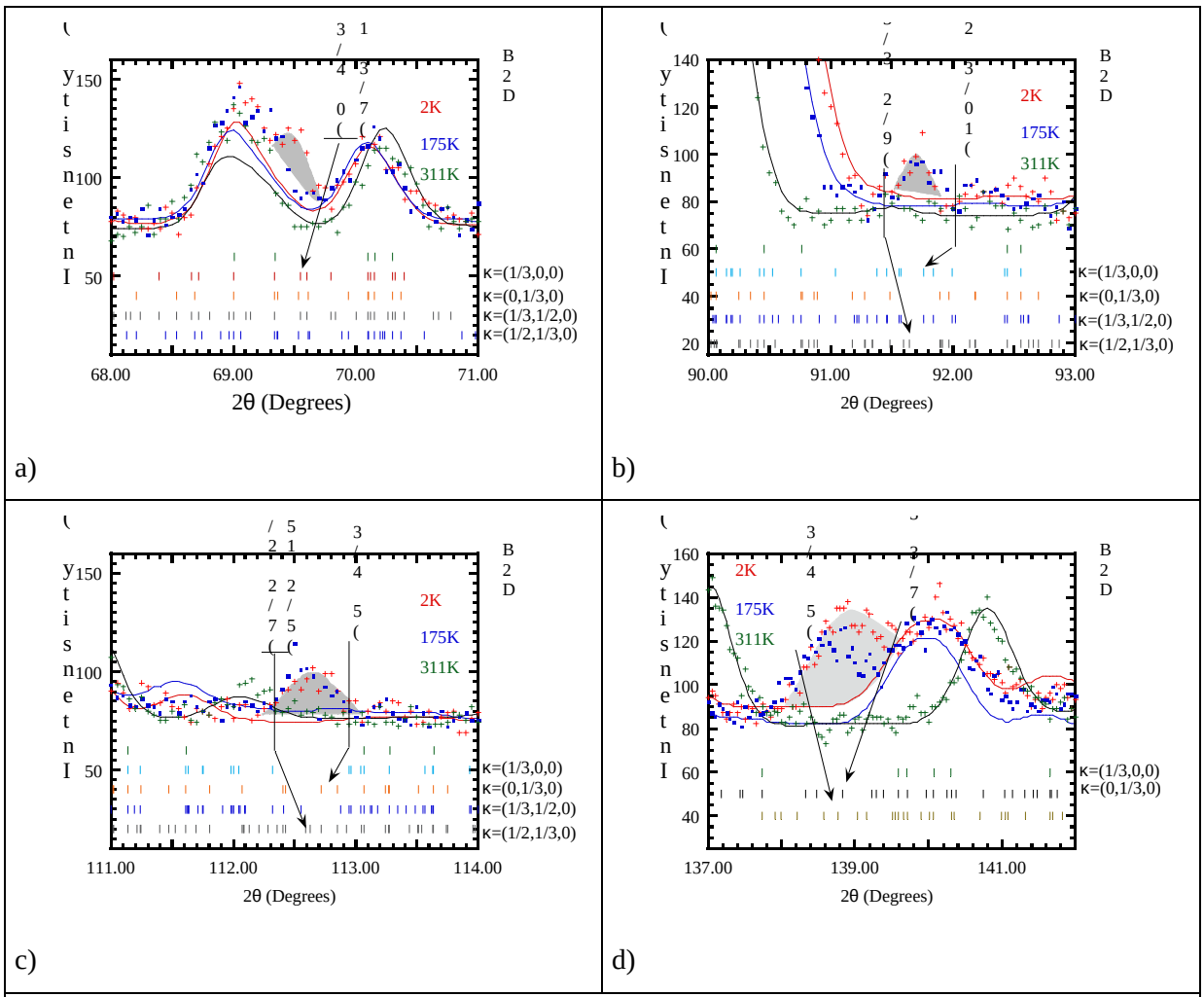

Fig. 8-34 *Superlattice peaks appearing on NPD (D2B) patterns below T_{CO} on $Bi_{1/3}Ca_{2/3}MnO_3$*

In conclusion, the ground state of $Bi_{1/3}Ca_{2/3}MnO_3$ compound consists in a quasi-degenerate state with different orbitally ordered domains coexisting at low temperature. The different domains have different coherence length depending on their structural modulation (Fig. 8-33). Hence, we concluded that the sample is composed by a series of domains, each having a different modulation vector and therefore a different orbital order. The domains are larger (2000 Å) for the phase of modulation vector κ_4=(1/2,1/3,0). Smaller domains (≈1000Å) are constituted by regions with κ_2=(0,1/3,0) structural modulation vector. In addition domains of about 800Å where found to

correspond to perpendicular structural modulation of the type κ_1=(1/3,0,0) and even smaller domains (400Å) where found to correspond to a bigger cell related to the latter κ_3=(1/3,1/2,0). Chen et al, [211] using high-resolution electron microscopy images observed charge ordered domains with perpendicular propagation vectors. The authors reported coherence lengths of the order of few thousand angstroms in size. Moreover, repeated thermal cycles did not change the charge ordering domains shape, suggesting that there exist strong pinning of the charge ordering domains to impurities or defects.

It is important to recall that at variance with lanthanum based compounds, $Bi_{1/3}Ca_{2/3}MnO_3$ compound exhibit large difference between the *a* and *b* cell parameters which has allowed us to perform a detailed study of the wave vector modulations in this compound using high resolution SXRPD and NPD data. If not such large difference existed it would have been impossible to resolve the structural modulations.

In the following section, the magnetic structure found at low temperatures is presented. In the light of the results of the coexistence of different orbitally order domains, we expect the coexistence of different magnetic structures which differ in the direction of the magnetic propagation vector.

Tab. 8-IX *Refined structural parameters from high resolution NPD and SXRPD data on $Bi_{1/3}Ca_{2/3}MnO_3$*

Parameter		2K-10K NPD+SXRPD	175K NPD	250K SXRPD	311K NPD	400K SXRPD
		Pbnm	Pbnm	Pbnm	Pbnm	Pbnm
a (Å)		5.36899(5)	5.3694(2)	5.37227(2)	5.3508(1)	5.35139(2)
b (Å)		5.40991(5)	5.4095(2)	5.40924(2)	5.3913(1)	5.38634(2)
c (Å)		7.44955 (6)	7.4660(3)	7.47854(3)	7.5345(2)	7.56556(3)
V ($Å^3$)		216.377(3)	216.85(1)	217.326(1)	217.358(8)	218.073(2)
ε_c		22.6	20.4	19.0	8	3
Bi/Ca	x	-0.0088(2)	-0.0073(5)	-0.0063(3)	-0.0034(5)	-0.0048(3)
	y	0.0403(1)	0.0404(4)	0.0392(1)	0.0374(3)	0.0365(1)
	z	0.25	0.25	0.25	0.25	0.25
Mn1	x	0.5	0.5	0.5	0.5	0.5
	y	0	0	0	0	0
	z	0	0	0	0	0
O1	x	0.0713(7)	0.0694(5)	0.074(1)	0.0701(3)	0.078(1)
	y	0.4837(7)	0.4844(4)	0.484(1)	0.4846(3)	0.4871(5)
	z	0.25	0.25	0.25	0.25	0.25
O2	x	0.7166(6)	0.7147(4)	0.715(1)	0.7133(3)	0.7113(7)
	y	0.2861(5)	0.2865(3)	0.283(1)	0.2872(3)	0.2894(6)
	z	0.0381(3)	0.0378(2)	0.0358(7)	0.0365(2)	0.0333(3)
R_p (%)		6.50	5.67	8.04	4.46	6.13
R_{wp} (%)		8.54	7.53	10.5	5.69	9.30
χ^2		4.42	2.99	7.56	2.02	8.01